CFD Analysis of a Linear Aerospike Engine with Film-cooling

A project presented to
The Faculty of the Department of Aerospace Engineering
San Jose State University

In partial fulfillment of the requirement for degree
Master of Science in Aerospace Engineering
San Jose State University

By

Paul Johnson

August 2019

Approved by

Dr. Periklis Papadopoulos
Faculty Advisor

Table of Contents

Figures

Abstract

The launching cost to send payloads into space is astronomical. Expanding the commercial space industry starts with lowering costs associated with the launch vehicle operation. Bringing down these costs begins with improving the propulsion systems, making these vehicles more efficient with a limited fuel capacity. The Linear Aerospike engine has demonstrated greater thrust efficiency over the current engines used on launch vehicles. However, unresolved issues with overheating plagues this design.

This study proposes a design alteration to the rocket motor, which explores how to reduce the operating temperatures of the nozzle body, and lower the possibility of failure due to the extreme thermal environments. Revitalizing the single stage to orbit concept eliminates the unnecessary weight of a secondary nozzle, control system, fuel and oxidizer tank, and second stage structure making the launch vehicle more cost efficient.

Studying how the main exhaust flow of a Linear Aerospike is affected by film-cooling, which entails injecting a cooling film layer between the exhaust flow and the interior walls of the nozzle; the study seeks to find a potentially viable solution to overheating. Using Star CCM+ CFD software, the study explores how secondary flow injection changes the exhaust flow characteristics, mainly velocity near the wall.

CFD results with and without film-cooling are analyzed. The results without film-cooling is used as a benchmark for comparing against previous CFD nozzle flow studies, to ensure the base geometry is not a contributing factor to the film-cooling results. The results show that equipped with singular injection nozzle, the injection of film-cooling secondary flow is insufficient to impact the boundary layer on the expansion ramp. However, the introduction of film-cooling had a negative effect on exhaust velocity.

Nomenclature

A	Nozzle Exit Area
a	Acceleration
A*	Nozzle Throat Area
$A_{total\ nozzle\ exit}$	Total surface area of the nozzle exit
A_ramp	Surface area of the expansion ramp
A_{base}	Surface area of the base
AR	Area Ratio (AR)
AR*	Equivalent Area Ratio
atm	Atmosphere
CFD	Computational Fluid Dynamics
CV	Control Volume
∇	Vector differential operator: Del operator
ΔV	Impulse per unit of spacecraft mass needed to perform an orbital maneuver
e_{energy}	Internal energy

F	Force
$F_{Propulsion}$	Force due to propulsion system
$F_{Pressure}$	Force due to Pressure
$F_{exhaust\ gas}$	Force due to exhaust gas
$F_{nozzle\ exit\ pressure}$	Force due to nozzle exit pressure
$F_{expansion\ ramp}$	Force acting on expansion ramp
$F_{nozzle\ base}$	Force acting on the spike base
g_0	Gravitational constant
γ	Isentropic Expansion Factor
I_{sp}	Specific impulse
k	Kelvin
λ	Bulk viscosity coefficient
M	Mass
m/s	Meters per second
$\dot{m}$	Mass flow rate
μ	Molecular viscosity
P	Pressure
P_c	Chamber Pressure
$p_{exhaust}$	Exhaust flow Pressure
P_e	Pressure at nozzle exit
P_a	Pressure Ambient
Pa	Pascal
psia	Pounds per square inch absolute
$\dot{q}$	Heat flow rate
ρ	Density
ρ_c	Density in chamber
T	Temperature
τ	Shear stress
θ	The angle between the center-line of the rocket and the center line of the primary nozzle exit
$v_{exhaust}$	Flow velocity at the primary nozzle exit.
V_{exit}	Velocity exit

1. Introduction

1.1 Motivation

1.1.1 The Problem at Hand

The cost to launch one kilogram of mass into orbit is about ten thousand dollars. Currently, launch vehicles require staging to inject payloads into orbital trajectories. These launch vehicles use the industry standard rocket bell nozzle. This requires having two or three additional propulsion and fuel systems for only one launch, adding production and complexity cost to the system.

In the future, reducing these high costs will need to come about through radical innovation to eliminate staging complexity and improve nozzle thrust efficiency, making launch vehicles less expensive and more energy efficient. Such innovation may be as simple as replacing the bell nozzle with Aerospike nozzle. This was the objective of the Single Stage to Orbit project, resulting in the development of the X-33 space plane and the Linear Aerospike rocket nozzle. The major advance that was driving research into the Linear Aerospike is the ability for the nozzle to adjust to the surrounding atmospheric pressure.

Contrary to conventional bell nozzles, which have a fixed area ratio optimized for a specific altitude, the Aerospike Nozzle is able to adjust the effective area ratio between the throat and the exit of the nozzle. This adjustability eliminates the need for rockets with multiple stages accompanied with additional nozzle and gimbal assemblies, reducing overall complexity.

Another benefit of this adjustability is that it enables the nozzles to operate at 100% of the theoretical thrust throughout the ascent of the launch vehicle, optimizing the fuel and oxidizer efficiency. Based on theoretical understanding and static testing data analyses, the Linear Aerospike nozzle showed promise to out-perform the traditional bell nozzle in specific impulse and thrust efficiency. Therefore, the Linear Aerospike rocket nozzle design has demonstrated the potential to both eliminate staging and improve overall engine efficiency.

Despite the performance advantages gained from using the Linear Aerospike Engine, financial and physical problems plague the design. The development of this engine cost the government well over a billion dollars, and they only performed a static test of the Linear Aerospike Engine. Meaning, future development of this engine will require significant financial investment. Additionally, engineers discovered a major issue with the operational environment of the Linear Aerospike. During the static fire testing, the extreme temperatures experienced by the major components, caused material degradation. Failures were not experienced during testing, however, these could develop into problematic failures later in the development. Ultimately the Single Stage to Orbit project discontinued due to the expense and engineering challenges.

Before the industry can benefit from the efficiency and performance of the Linear Aerospike, there are several logistical barriers and engineering problems that still need to be solved. For one, the Aerospike Nozzle has never been flown on a large-scale rocket platform capable of reaching orbit. Second, the Aerospike nozzle has very high production costs and problems with heat dissipation.

1.1.2   Reason for Pursuit

Making the Aerospike nozzle a practical replacement for the bell nozzle in launch vehicles means improving the capabilities of the space industry. Increasing the performance of the propulsion system correlates to drastic increases in the mass capacity of the launch vehicle. This performance increase means the space industry can benefit from lower launching costs, making profitability more appealing for competition to enter the market, leading to industry growth. By manipulating the rocket equation (1.1) and isolating the mass terms on one side, it is evident that adjustments to the specific impulse result in exponential changes to the launch vehicle mass ratio. The ratio being, the initial launch vehicle mass over the final launch vehicle mass after the rocket motor has burns out.

$$\Delta V = I_{SP} * g_0 * \ln \frac{Mass_{initial}}{Mass_{Final}}$$

$$\frac{\Delta V}{I_{SP} * g_0} = \ln \frac{Mass_{initial}}{Mass_{Final}}$$

$$\frac{Mass_{initial}}{Mass_{final}} = e^{\frac{\Delta V}{I_{SP} * g_0}}$$

$$\frac{Mass_{initial}}{Mass_{final}} = e^{\frac{\Delta V}{I_{SP} * g_0}}$$

$$(1.1)$$

Improvements to the propulsion system allow for more mass to be sent into space for the same amount of energy or expend less energy to send the same amount of mass into space. By developing solutions to the issues plaguing the Aerospike Nozzle, the engine could be adopted into future launch vehicle platforms and allow the aerospace industry to exploit the design efficiencies for financial benefit.

1.2   Literature Review

After performing research, nothing was found regarding use of film-cooling as a method to lower heat flux into the body of a Linear Aerospike nozzle. Hence, the following literature review addresses past film-cooling studies, supersonic fluid interactions, as well as the geometry and specifications of the Aerospike Nozzle.

1.2.1 Film-cooling

The Author performed an extensive literature review of journal articles and research papers about film-cooling methods. The application of film-cooling that centered his research was used for cooling jet turbine blades. A thorough literature review was performed; over thirty bodies of research were reviewed and evaluated on film-cooling methods either experimental or simulated results.

The literature research revealed the commonalities and strengths of the chosen articles. The author evaluates the important CFD practices and presents optimal film-cooling injection port orientation [1]. The literature review presented in the paper, provides an overview of film-cooling. This paper validates the use of film-cooling in environments with high heat and turbulent flow. These methods and results will assist with the development of the injection port geometry for the Linear Aerospike Nozzle later discussed.

Song [2] experimented with flow visualization of tangentially injected film-cooling in supersonic flow. Aside from flow visualization, the journal addresses how the flow field is affected by changes in film-cooling injection pressure. Mach number of the free-stream flow is set at Mach 2.95, using a continuous suction wind tunnel. In the test section, a 90 degree step has backwards-facing injection ports were oriented tangentially to the free-stream flow direction. The injection port is modeled after a Half-Laval Nozzle, producing an exit flow velocity of Mach 1.5.

The results illustrated that in fact the feed pressure of the film-cooling gas had a big effect on the free-stream flow behind the step/injector nozzles. The film-cooling changed the expansion fan and oblique shockwave produced from the upper edge of the step and nozzle. The experimental results corroborated CFD simulations for similar backwards-facing film-cooling configurations.

The research presented in Song [2] this journal article will assist with characterizing how the rocket plume produced by the Linear Aerospike will be affected by secondary flow injection. The shockwaves and other flow characteristics will be observed in the Aerospike CDF Simulation.

Shewhart, et al[3], explored ways of mitigating the possibility of unburned fuel from the combustion chamber traveling into the hot turbine section producing a secondary reaction.

The above team presented two secondary reaction mitigation techniques, which are to be implemented on a jet engine. One employed film-cooling on the turbine blades to cool the turbine environment. The second method used the wall to buffer the reactions and reduce the local augmentation and subsequently the heat load generated. Experimental data is capture from well-stirred reaction testing. Four different film-cooling configurations were developed, for each configuration a different coolant injection angle and combination is tested. Also, both nitrogen and air were evaluated as injector fluid. To capture heat flux data, thermocouples were placed at even incremental distances behind the film-cooling injection locations. A camera placed beside the test section captured visuals illustrating the interaction between the free-stream and the injected flow.

The results obtained supported the hypothesis that film-cooling would reduce the heat flux. Additionally, the results showed that a rolling injector configuration was optimal for reducing heat flux using enhanced mixing.

The other successful configuration was a five-slotted configuration. They were able to reduce the heat flux by 60 percent under certain conditions using air and nitrogen as the

injector fluid [3]. The results of the study will be utilized with the coolant injector design. The heat flux reduction data will be evaluated for the design integration on the Linear Aerospike geometry. This provides visual data for comparison in the CFD results for the film-cooling flow interaction.

At RWTH Aachen University, Hombsch [4] performed experiments with film-cooling techniques on a flat plate in supersonic flow. In the analysis both Laminar and turbulent boundary layers regimes are examined. During the experiment, parameters such as injection angle and coolant mass flow rate were varied. The objective of the study was to capture data on the cooling effect and develop a relationship to the adjustable parameters, in other words cooling efficiency. In the test section of the supersonic wind tunnel, Four different wedge configurations were tested. These wedges were used as the flat plates, using the wedge angle and incident Mach number to manipulate the flow conditions over the film-cooling section.

One configuration for the laminar regime consisted of secondary flow injection ports oriented 10 degrees away from the flow direction with a pressure rake and thermocouple to capture the boundary layer data. The other configuration, used for the turbulent flow regime, was equipped with sandpaper to trip the flow and cooling ports oriented 45 degrees to the flow direction for the secondary flow injection. In both cases a color Schlieren was used to capture the flow density variations. The cooling efficiency was found to increase as the angle between the cooling flow injection and the free-stream flow direction decreased.

Additionally for the turbulent case they discovered, increasing the mass flow rate correlated to increased cooling efficiency, which makes sense due to more cooling fluid being introduced [4]. The article addresses film-cooling and its application in traditional bell nozzles. They address how one would model the flow to simulate rocket nozzle flow. This research will assist with generating the secondary flow injection ports on the expansion ramp.

Aerospace industry professional from Wright-Patterson Air Force Base and Edwards Air Force Base, evaluated cooling methods for a rocket nozzle and combustion chamber. Film-cooling was identified as a viable cooling method for the body of research. Instead of air or an inert gas as the fluid medium for cooling, liquid fuel was injected along the surface.

Using CFD the above authors modeled the fuel cooling method along a flat plate using CFD software package with turbulent multiphase flow computation abilities. The flow is modeled as a chemically reacting flow, which accounts for energy released when the free-stream interacts with the fuel rich boundary layer. Cooling channels imbedded in the plate inject fuel-coolant into the free-stream.

The results of the CFD analysis for non-chemically reacting flows showed that heat flux into the body decreased by a maximum of 3 percent. Results also revealed that using fuel as a cooling medium with chemically reactivity taken in to account, increased the flow temperature near the wall.

This seems appropriate given that fuel is stored chemical energy, and when it introduced to a heat source like high-speed flow; the energy will release in the form of heat and kinetic energy [5]. This research provides good insight into film-cooling. This was one of few articles where film-cooling was discussed in a rocket nozzle application. The fuel medium as a cooling method was not successful. However this might provide means for producing more thrust from the Linear Aerospike Nozzle platform.

Schneider [6] analyzed the flow exhausted from a dual-bell Nozzle. The dual-bell nozzle is designed to "adjust" to changing altitude conditions. The nozzle has two different area ratios, changing a specified distance aft of the throat. Before the transition event, aspiration drag is present accompanied by an adverse pressure gradient in the larger area section of the

nozzle. Secondary flow injection, film-cooling, was presented as a method to mitigate this drag and provide nozzle cooling. Numerical simulations for a nozzle with and without film-cooling were created using a CFD fluids solver. Additionally, A dual-bell nozzle with and without integrated film-cooling was constructed to capture cold flow experimental data to validate numerical models.

Results from the experimental and CFD analysis illustrated that film-cooling was able to increase the Nozzle Pressure Ratio (NPR) range, at the location of transition. Typically this corresponds to a significant dip in thrust coefficient, however, with film-cooling the numerical and experimental data showed the dip was diminished. The film-cooling effect was dependent on the secondary flow injection pressure. The CFD solutions results show a mild suppression of the main jet from the film-cooling flow. The higher film-cooling pressures resulted in the flow transitioning at lower nozzle pressure ratios [6]. The application of film-cooling in a nozzle flow, despite only being a small scale cold flow experiment and a CFD numerical solution, validates the possibility of applying this method in a nozzle.

1.2.2   Flow Injection into Supersonic Flow

In the late 1960's, Street [7] performed secondary flow injections experiments in supersonic wind tunnel. The free flow velocity was set at Mach 2.56 and the secondary injection flow pressure ratio was varied between 3.2 and 28 .6. Four different nozzle designs were explored, sonic and supersonic, and injection normal and at 45 degrees downstream. Static pressure data was captured on the wall adjacent to the flow injectors inside the wind tunnel test section. A pressure and concentration profile of the wake aft of the injectors was captured for analysis.

The experimental data was used to develop scale parameters based on analytics of the flow field, later verified by experimentation. The optimal cooling configuration was found to be injecting in the upstream direction using a supersonic nozzle. The optimal design for least flow disturbance was the sonic flow with a 45 degree downstream injection [7]. The research performed in the study will be considered when developing the injector conditions on the expansion ramp. This article brings to question what would work best in a nozzle application upstream versus downstream injection, and sonic versus subsonic flow velocities.

Zukoski and Spaid [8] investigated the resulting flow field interactions caused by injecting secondary flow into supersonic flow. The objective was to inject flow normal to the free-stream and study how the gases interact. The tests were carried out in a supersonic wind tunnel facility at Cal Tech. the free-stream Mach numbers were varied between 1.38 and 4.54. The single injection port was oriented 90 degrees from the free-stream on a flat plate in the center of the test section. The inert gases nitrogen, argon, and helium were used as injectants, to ensure no energy was released or introduced into the experiment via a chemical reaction.

The study gave the scientific community new data regarding pressure fields, concentration fields, and shock wave shape. From data compiling and calculations, the authors developed a scaling parameter that can be used to predict side forces generated by the introduction of a secondary flow. This scale parameter was in agreement with existing rocket motor tests and thus adds validity to the results [8]. This was one of the first flow injection studies ever conducted, and produced a ton of literature on flow interaction. This information is will aid in theoretical analysis of introducing film-cooling on the expansion ramp of the Linear Aerospike.

Wang [9] researched how adding an engine fence to the X-33 Linear Aerospike nozzle would change the heat flux to the body. The proposed addition of a fence to the ends of the Linear Aerospike engine would in theory mitigate some of the base heating radiation generated from the nozzle's plume during ascent. To capture the heat radiation, the author used a three dimensional thermo-flow-field that accounts for the geometry of the entire vehicle. The purpose of generating a three dimensional model is to ensure they accurately capture the flow spillage and see how the flow interacts with the X-33 Geometry. They employed finite differencing, viscous; chemically reacting, pressure-based CFD formulation and a finite volume, as well as radiation heat transfer methods to accurately simulate the heating.

In all, 15 simulation conditions were tested, with and without the fence, and with and without base bleeding effects. The CFD simulation solutions were verified and compared with scale model hot flow tests. Heating data at specific locations on a 2.25 percent scale model of the X-33 were captured and compared to a 2.25 percent scale CFD simulation. The data from the experimental testing paralleled the results from the CFD simulations [10]. The source provides good information on the simulation environments. CFD, radiant heating equations (GRASP), chemically reacting flows, and heat flux information were provided in detail. The information will be utilized for generating the CFD solutions in the following study.

Sutton [11] provides a comprehensive background on the functionality of the Linear Aerospike design. Sutton spent his engineering career in the propulsion industry, working for Rocketdyne and Rockwell International. Ultimately he ended his career as an engineer at Lawrence Livermore national laboratory. Although Sutton was not a contributing member in the development of the Linear Aerospike, he is an expert in the field of propulsion and has authored numerous texts on rocket propulsion [11]. This source provides an overall background knowledge of the Linear Aerospike and the benefits and limitations.

1.2.3   Shockwave Interaction

Amjad [12] employed research from a previous study on separation bubble formation, for developing a method for analyzing a turbulent boundary layer and shockwave interaction in a compression corner. Utilizing the prior research, they used a shockwave unsteadiness modification to develop methods for turbulent boundary layer and oblique shockwave interactions. A CFD solver used the Favre-Averaged Navier-Stokes equation from a sourced paper and the corrected k-omega turbulence coefficients for shock-unsteadiness to solve the coupled second order flow equations.

The initial flow conditions were set to Mach 5, temp of 68.3 kelvin, and an atmospheric pressure of 4008.5 Newton's per meter squared. In the test section of the simulation they had a wedge that producing the oblique shockwave, and they had a flat plate below to provide the boundary layer for impingement. The addition of the of the correction factor into the k-omega turbulence equation resulted in a more robust solution. The predictions for the turbulent flow model cases were greatly improved, the results of the simulation showed a greater resemblance to experimental results [12].

The research presented provides an equation that produces more realistic simulation results. The turbulent flow and reflected shockwaves produced during operation of the Linear Aerospike will depend on a correction similar to the one presented to produce credible results. Additionally with the added film-cooling, simulation accuracy capturing the shockwave and boundary layer interactions will be pivotal to the success of the simulation.

Sandham [13] from the aerodynamics and flight mechanics research group in Southampton, UK studied the shockwave and boundary layer interaction (SWBLI) in supersonic flow. The objective of the article was to gain an understanding of the physical phenomena that develop in simplified model problems for such interactions. The simulation models developed for this study included Large-Eddy Simulation (LES) code to capture the turning flow inside the separation bubble generated from the SWBLI. From experimentation, flow visualization data from the Particle-Image-Visualization (PIV) software.

The simulation data was compared to previous experimental data for shock impingement on a flat plate. The LES and PIV results were compared and showed similar results for velocity as a function of distance from the flat plate. The research will be utilized when analyzing the flow inside the plume of the Linear Aerospike computational model [13]. The SWBLI between the film-cooling layer and the reflected shockwaves inside the exhaust flow will behave similarly to the flow examined in the research article.

Borovoy et al [14], studied shock-to-shock interactions via wind tunnel experimentation. Numerical and experimental results were both presented for shock-to-shock interactions in near the wall flow due to blunt and sharp bodies. The free-stream Mach number was varied between 5 and 10, and the Reynolds number varied between 0.3 and 27 x10^6 corresponding to laminar and turbulent boundary layers.

The leading edge of the bluntness variation on the plate resulted in alterations in heat transfer due to an increased separation zone and reduced gas density. This changed the characteristics of the interference region. The increased bluntness resulted in greater heat transfer decay, meaning the bluntness correlated to lower heat exchange and lower flow temperatures near the body [14]. Due to the nature of the Aerospike nozzles, oblique shockwaves are present in the plume flow. With film-cooling being essential the introduction of a thin cool boundary layer, shock-to-shock interactions will occur on the expansion ramp. Thus, a strong understanding on what occurs during the interaction between these flow-components is vital to the analysis. This resource provides insight on these flow phenomena.

1.3   Project Proposal

The overall objective of the study is to investigate if the addition of film-cooling to the expansion ramp of the Aerospike nozzle introduces a thermal boundary layer near the body of the nozzle without detracting from the performance.

Film-cooling is a method employed on hypersonic vehicles, speeds greater than Mach 5, to cool the body or airframe of the vehicle. The technique involves injecting fluid into the high-speed flow adjacent to the surface of the body of the vehicle, creating a boundary layer of cool flow acting as insulation, ultimately reducing the heat flux that enters the body.

Therefore, the objective of the project is to use Computational Fluid Dynamics (CFD) to analyze a Linear Aerospike Nozzle with the addition of film-cooling. The results will show how the propulsion characteristics of the nozzle are affected by the addition of film-cooling along the expansion ramp.

1.4   Methodology

With the expensive nature of propulsion projects, requiring capital to manufacture such system, fluid simulation software shall be utilized to analyze the performance of the nozzle. The fluid simulation software StarCCM+ will be employed to perform the analysis. The first

step in the analysis will be to develop the Aerospike computational geometry and compare the CFD results with other papers analyzing the Aerospike nozzle using CFD software. This will provide a foundation for analyzing the addition of the film-cooling flow injection, establishing that the geometry is congruent with the results of other studies and not contributing to the film-cooling results.

After validating the geometry, the secondary flow injection will be added to the model at a specific location along the expansion ramp of the nozzle. That position will be determined once the flow characteristics are investigated and analyzed based on preliminary research and CFD simulation results. The geometry will be similar in nature to the XRS-2200 Linear Aerospike as seen in a preliminary sketch in Figure 1.4.1.
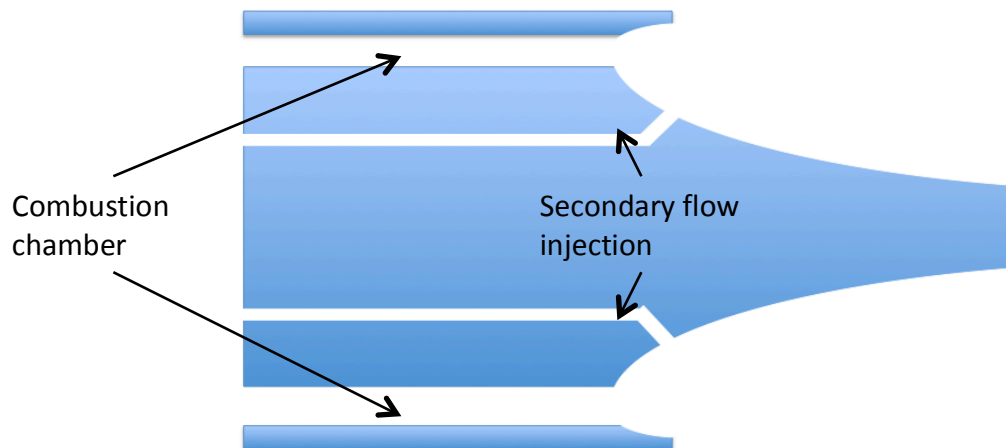
Figure 1.4.1 – Preliminary 2D-sketch of the Linear Aerospike Nozzle Geometry.

Since the objective of this study is to analyze the fluid flow characteristics of the exhaust plume with film-cooling, the conditions in the main and injection nozzle combustion chamber are set up for cold gas. The nozzle is developed using previously published data and methods, described in detail below. A benchmark analysis will be performed on the expansion ramp geometry, comparing the results to previously published studies. Ensuring the pressure value determined for the chamber are within a feasible range, data from the XRS-2200 Aerospike test fire is gathered for comparison. For the initial conditions the study will source previously published data that serves as a benchmark to test the geometry.

2.   Overview of the Aerospike

2.1 Aerospike Nozzle Design

The Aerospike rocket engine was first conceptualized in the quest for innovations to reach orbit using only one stage. After years of research and development, prototypes of this unique nozzle were finally fabricated and test fired in the 1990's.

The Aerospike nozzle concept was developed by fundamentally inverting the traditional bell nozzle profile. This nozzle design became known as the toroidal Aerospike nozzle, shown in Figure 2.1.1, because the bell profile is circularly revolved about the axis of symmetry of the rocket. Despite the alien appearance of this nozzle design, this nozzle has all the elements of a traditional convergent-divergent nozzle. Instead of having the traditional large

convergent section, funneling the high-pressure gases centrally towards the throat, the Aerospike nozzle forces the gases toward the outer edge of the vehicle where the annular "throat" is located.

The throat of the Aerospike has non-traditional geometry and location but functions the same as traditional nozzle throat. The throat being the smallest cross sectional area is located on the outer edge of the nozzle geometry, instead of being at the center of the nozzles axis of symmetry. From the choked flow at the throat, the flow moves through a divergent section, where it is expanded and accelerated against the nozzle structure to supersonic velocities. Having the exhaust gases funneled towards the center line of the rocket allows greater thrust force efficiency because the expanded gases are aligned with the rocket instead of flaring outward away from the rocket, such is the case with the bell nozzle.

The spike nozzle structure to which the flow is expanded against functions the same as the traditional bell nozzle, despite its non-traditional appearance. This spike feature gives the Aerospike nozzle a major operational advantage over the bell nozzle because one of the divergent "surfaces" is dynamic.

With the traditional bell nozzle design, the divergent surfaces of the nozzle are fixed and surround the flow as it expands along the bell curve. The Aerospike however, has the expansion surfaces on the interior of the flow, leaving elements of the expanding flow exposed to the free-stream flow around the launch vehicle. Interactions between the exposed exhaust flow elements and the free-stream flow are what give the Aerospike nozzle a dynamic advantage over the bell nozzle counterpart.

The Aerospike utilizes atmospheric pressure surrounding the nozzle to aid with accelerating the hot exhaust gases through the divergent section and generate thrust. The atmospheric pressure compresses the flow against the walls of the toroidal spike accelerating the sonic gases to supersonic speeds [15]. More technically speaking, this phenomenon is known as the universal law of diffusion. When the high-velocity low-pressure exhaust flow encounters the high-pressure of the atmosphere, the natural laws of fluid mechanics dictates that higher-pressure flow will seek to occupy regions occupied by lower pressure flow.

As previously mentioned, the dynamic capabilities and altitude compensation is the major advantage of the Aerospike nozzle. Having fixed nozzle geometry, such as with the bell nozzle the area ratio must be designed for a specific altitude. Evaluation of the area ratio equation below, Equation (2.1.1), When the area ratio is held constant, the pressure and density variable for the exit conditions must also be held constant as well for the equation to hold true. Having fixed nozzle geometry, the area ratio must be designed for a specific altitude.

This means that during the initial stages of the ascent the exhaust flow is over expanded, allowing for an adverse pressure gradient to separate the flow from the nozzle surfaces near the nozzle exit. Then at a certain altitude the flow will become ideally expanded and the flow will remain attached. This ideal flow condition occurs precisely when the variables for pressure and density in Equation (2.1.1) below, result in the same area ratio as the nozzle. This means during a majority of the vehicles ascent, the bell nozzle is underperforming. The thrust efficiency is less than 100 percent.

The Aerospike, having a dynamic divergent section, means the nozzle has a dynamic area ratio. This variability translates to the pressure and density variable for the exit conditions can also be varied. With the outer jet boundary of the exhaust flow adjusting to altitude, the effective area ratio (AR) adjusts in flight to atmospheric conditions [20]. The

adjustability of the diffused boundary, as seen in Figure 2.1.2, which means the flow is ideally expanded throughout the ascent. This nozzle is functioning at 100 percent thrust efficiency.

$$\Gamma(\gamma) = \sqrt{\gamma \left(\frac{1+\gamma}{2}\right)^{(1+\gamma)/(1-\gamma)}}$$

$$AR = \frac{A}{A^*} = \cfrac{\Gamma(\gamma)}{\sqrt{\frac{2\gamma}{\gamma-1}\left(\frac{\rho}{\rho_c}\right)^{2/\gamma}[1-\left(\frac{p_a}{p_c}\right)^{\frac{\gamma-1}{\gamma}}]}}$$

(2.1.1)
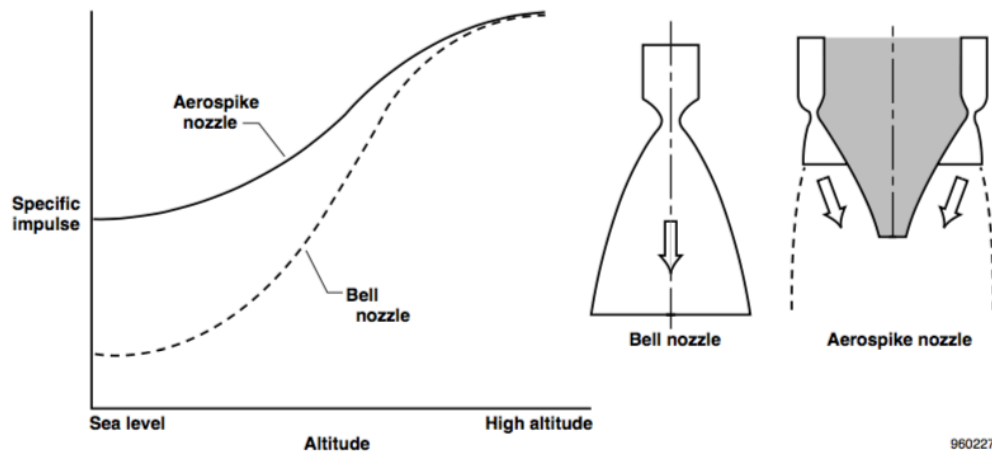
Figure 2.1.1 – How specific impulse changes with altitude for the Aerospike nozzle and the Bell nozzle [16]

Specific impulse is a metric that relates the thrust generated from the gas combustion process and how much fuel was used during the process. This can be thought of as fuel efficiency; the higher the specific impulse, the more efficient the engine is at converting the fuel into thrust.
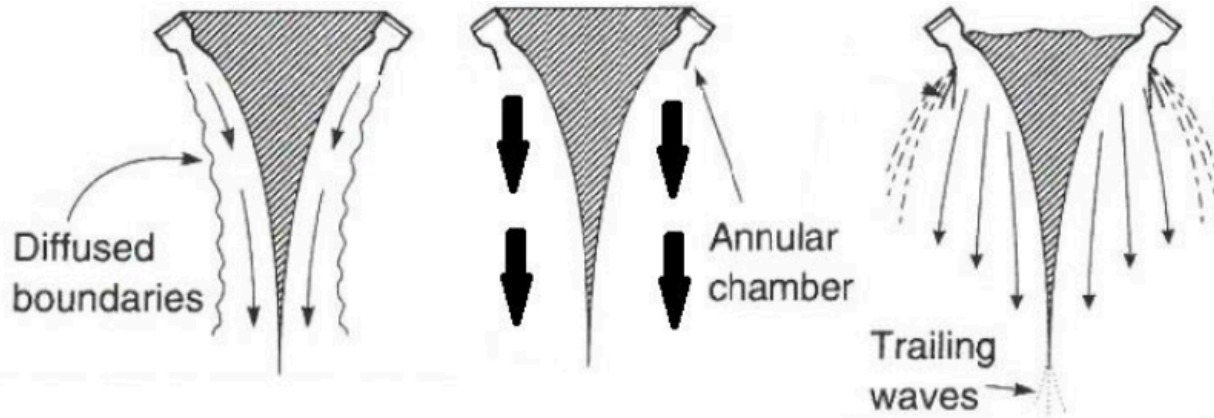
Figure 2.1.2 – Toroidal Aerospike [17]

The force equations of the Aerospike nozzle have two components contributing to thrust generation. One describes the force from the nozzles expelling the combustion chamber gases to supersonic velocities. The second component accounts for the pressure acting normal to the expansion ramp surface. Equation (2.1.2) is integrated from Sutton's textbook on propulsion [11] and is modified for the spike case.

$$F = F_{Propulsion} + F_{Pressure}$$

$$F = \left[F_{exhaust\ gas} + F_{Pressure\ nozzle\ exit}\right] + \left[F_{toroidal\ Spike}\right]$$

$$F = [\dot{m}v_{exhaust}cos\theta + (p_{exhaust} - p_{ambient})A_{total\ nozzle\ exit}cos\theta]$$

$$+ \int^{A_{spike}} p dA$$

(2.1.2)

The $\dot{m}$ term refers to the mass flow rate of the exhaust gases leaving the throat or primary nozzle at the top of the ramp. The $v_{exhaust}$ term refers to the flow velocity at the location of the primary nozzle exit. The θ term is the angle between the centerline of the rocket and the centerline of the primary nozzle exit. The first delta, $p_{exhaust} - p_{ambient}$ describes the pressure difference between the atmospheric pressure and the pressure at the nozzle exit. This pressure difference is multiplied by the total area of the nozzle exit area, adjusted for the angle between the normal vector from the nozzle exit and with the rocket centerline. The last area integral term accounts for the pressure distributed over the surface of the spike. This pressure is generated form the low-pressure flow near the spike geometry and the high pressure surrounding the low-pressure flow.

Instead of having a long toroidal spike protruding from the launch vehicle, for sizing needs or manufacturing feasibility, truncation of the spike may be warranted. Truncation of

the spike does not detract from the performance of the nozzle. As aforementioned, optimization research has shown that an Aerospike nozzle with a 40 percent truncation yields the greatest exit velocity [15]. Truncation of the spike creates a small region of recirculating flow at the base of the nozzle. This recirculating flow is caused by increases the pressure on the base and contributes to the thrust force.

Characterization of the nozzle flows can be broken down into regions of supersonic and subsonic flow. These regions are separated by fluid boundaries, these jet boundaries and shear layers provide an interacting medium for the flow to exchange momentum from supersonic to subsonic. The outer jet boundary is the outer most boundary that separates the region above the envelope shock from the free-stream flow. This region above the envelope shock has compression shockwaves slowing down the flow, however the flow is still supersonic. On the n -Below the envelope shock the flow is supersonic. From the sonic flow conditions at the throat, the exhaust gases passes through a series of expansion waves generated from the lip of the primary nozzle.

The series of expansion waves accelerates the flow as it moves down the expansion ramp. On truncated spikes, a shear layer exists between the supersonic exhaust gases and the subsonic recirculation region aft of the base of the spike. In this shear layer, viscous effects slow down the adjacent flow creating flow circulation. This circulation pulls some of the exhaust flow in to the subsonic region at the base of the spike. Emanating from this inner shear later shear layer a trailing shockwave bisects the exhaust flow and creating an oblique shock that results in the pressure behind equal to ambient pressure.
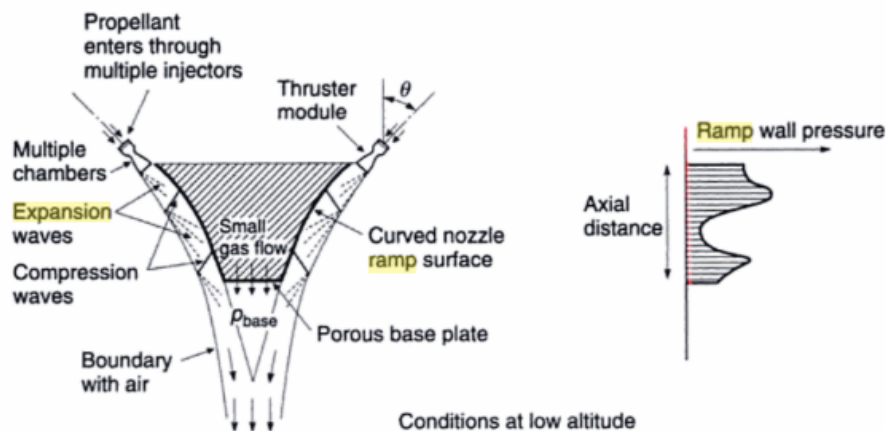
Figure 2.1.3 – Truncated nozzle at low altitude [11].

Figure 2.1.3 provides an illustration of the flow regions on the expansion ramp of the nozzle.

2.2 Linear Aerospike

The Linear Aerospike XRS-2200 was designed for the SSTO space plane known as the X-33. Fundamentally, the Linear Aerospike functions the same as the toroidal Aerospike because taking a two-dimensional cross section of the original toroidal concept and extruding the profile normal in the third dimension yields the geometry of the Linear Aerospike.

The main difference between the two types of engines is the combustion chamber design. Instead of a single annular combustion chamber and throat like the toroidal engines, the Linear Aerospike used small rectangular combustion chambers forcing the high-pressure combustion gasses towards a rectangular throat. These chambers are mounted at the top edge of the spike, and in total there are 20 individual chambers, 10 on each bank of the Spike. Bringing the potential for modularity, scaling the engine to the size of vehicle. Having two distinct sides enables each side to be throttled differently, which in theory could be used to induce rolls, pitch, or yaw the launch vehicle. This ability provides another aspect to the fight computer for controlling the trajectory of the rocket.
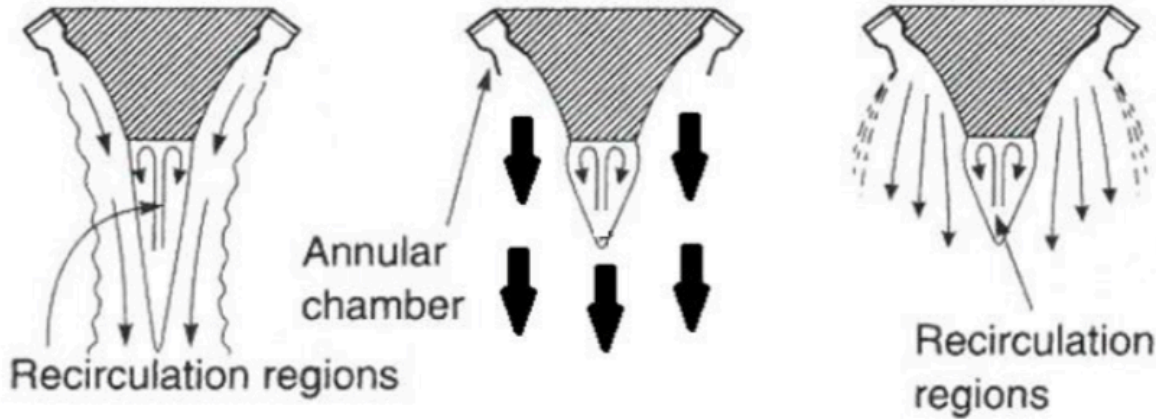
Figure 2.2.1 – Aerospike Nozzle with a truncated base [17]

The Aerospike Nozzle force equations have two components contributing to generating thrust. One describes the force from the nozzles expelling the combustion chamber gases to supersonic velocities and the pressure difference on the nozzle exit area. The second component accounts for the pressure acting normal to the expansion ramp and base surfaces.

$$F = F_{Propulsion} + F_{Pressure}$$

$$F = \left[F_{exhaust\ gas} + F_{nozzle\ exit\ pressure}\right]$$
$$+ \left[F_{expansion\ ramp} + F_{nozzle\ base}\right]$$

$$F = [\dot{m}v_{exhaust}cos\theta + (p_{exhaust} - p_{ambient})A_{total\ nozzle\ exit}cos\theta]$$
$$+ 2\int^{A\_ramp} pdA + (p_{base} - p_{ambient})A_{base}$$

$$(2.2.1)$$

This force equation describing the thrust of a Linear Aerospike is similar to the equation for a spike nozzle. The last term, $p_{base} - p_{ambient}$ accounts for the pressure distribution on the bottom of the truncated section of the nozzle [11]. The pressure component of the base can be increased if the exhaust gases from the turbo pumps are routed to exit the system out of the end of the expansion ramp into the region of recirculation. Rerouting the exhaust through the base is a method known as base bleeding, shown in Figure 2.2.2.
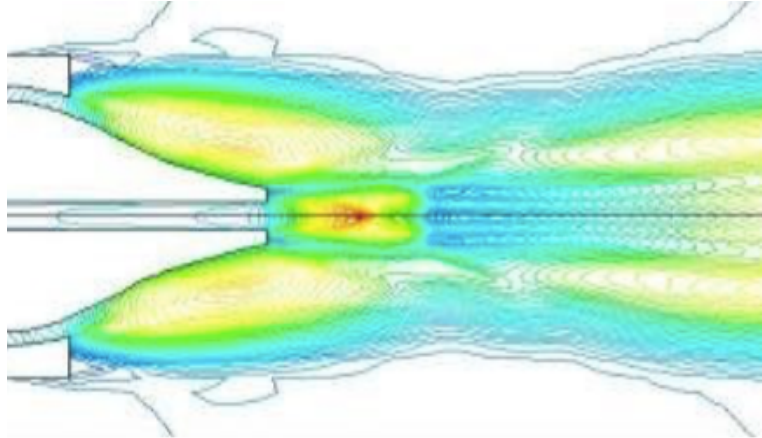
Figure 2.2.2 – The Aerospike expansion ramp curvature [15]

2.3   Problem

As previously mentioned, one major issue with the design, which was uncovered during static fire testing of the Linear Aerospike, is the difficulty with heat dissipation. The main component responsible for flow expansion is the expansion ramp. Immediately aft of the combustion chamber, the hot gasses are expelled at temperatures around 3000 kelvin. These hot gasses, still smoldering at around 1500k, bombard the expansion ramp for roughly eight minute during the ascent phase of the launch.

This thermal environment poses as a potential point of material failure. Cooling lines, filled with cryogenic fuel and oxidizer placed on the back of the ramp provide a form of cooling through conduction. However, more cooling efforts are warranted to reduce the temperature of the wall. Providing a barrier between the flow and the body, film-cooling may be a solution to lower the temperatures experienced by the body.

3.   Aerospike Design

3.1 Geometry

3.1.1   Aerospike geometry

The primary step of the analysis begins with defining the necessary assumptions to simplify the problem without compromising the accuracy of the results. These assumptions

will be implemented in the setup of the CFD solver. The following details assumptions that will be applied to the analysis.

The nozzle will be assumed set at a specific altitude, meaning the ambient pressure in the environment around the nozzle will be fixed. This assumption is valid for this analysis because variations in ambient pressure affect the distance between the boundary regions of the plume and the walls of the expansion ramp. The CFD results with added film-cooling should be unaffected by boundary region location. The altitude will be at sea level, simulating a static fire ground test.

3.1.1.1   Nozzle Shape - Secant Method

The most important component of the Aerospike is the expansion ramp. The ramp shape is important for gas expansion and minimizing total pressure losses downstream of the nozzle. The secant method was employed to define the nozzle contour. This method involves performing iterations with the Prandlt-Meyer expansion wave theory equations.

A MATLAB script performs the method after each iteration and the output generates a text file with two-dimensional xy-coordinates. These coordinates were entered into a Computer Aided Design program provided by Solidworks, where a solid geometry of the nozzle was developed. From there, the geometry features of the base and initial nozzles that line the upper cowl of the expansion ramp are added as flat surface geometry.

Mach angle and Prandlt-Meyer expansion wave theory were employed to generate the geometry of the expansion ramp. The following assumptions need to be made before employing this method. The flow exiting the nozzle is steady, irrotational, isentropic, and neglect viscous effects. Additionally, the expansion waves that are impacting the expansion ramp are assumed to be straight lines. Finally, the conditions at the throat are assumed sonic.
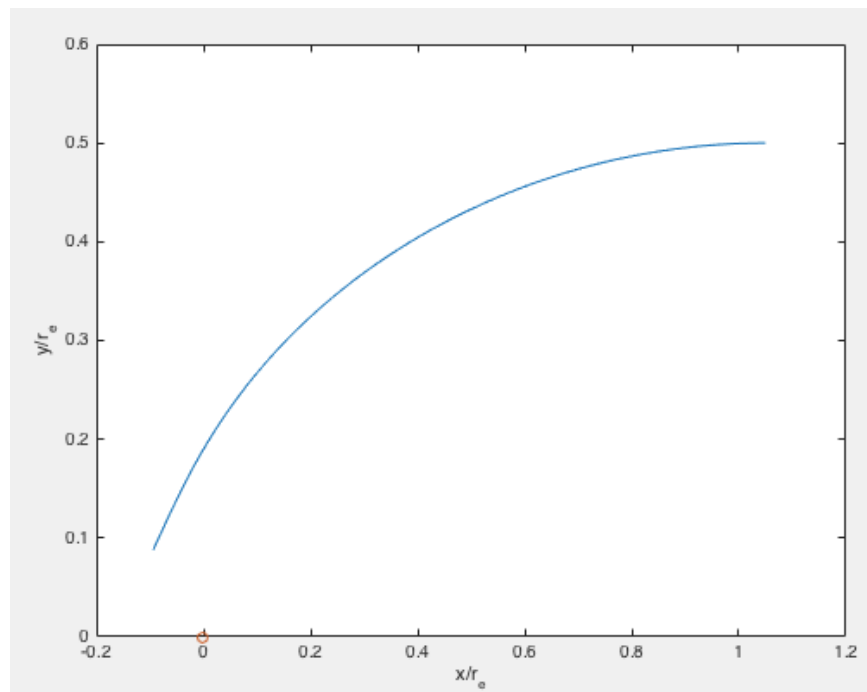
Figure 3.1.1.1.1 – The Aerospike Expansion Ramp Curvature

3.1.1.2   Base Bleeding

Base bleeding is where the exhaust gases used to power the fuel and oxidizer pump are diverted out through the base. This engine feature generates a greater pressure difference at the base generating more thrust. The Base of the truncated Aerospike will not include base bleeding in the analysis [15].
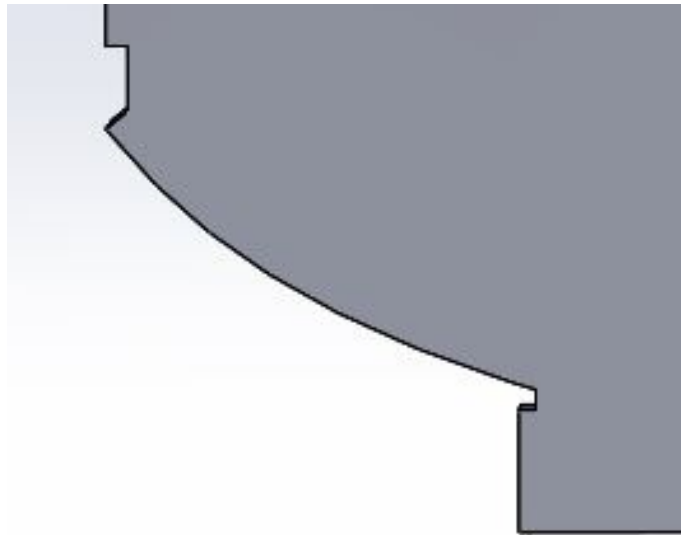
Figure 3.1.1.2.1 – CFD geometry of the Aerospike with base bleeding visible

3.1.1.3   Nozzle Dimensions

Since the XRS-2200 Linear used by the X-33 is the model for the Aerospike used for the following analysis, the dimensions and specifications of that engine are as follows.

The pressure in the combustion chamber was measured at 854 psia, which equates to roughly 58 atm. The fuel used for this engine was a mixture of liquid hydrogen and oxygen, with a fuel to oxidizer ratio was 5.5:1. The truncated base of the Linear Aerospike is 46 inches wide. The width of the Aerospike at the top of the expansion ramp is 134 inches measured from one bank to the other. The depth of the expansion ramp is 88 in, however since the analysis is two-dimensional this geometry parameter will be neglected. Refer to Figure 3.1.1.3.1 for a better understanding of the dimensions.
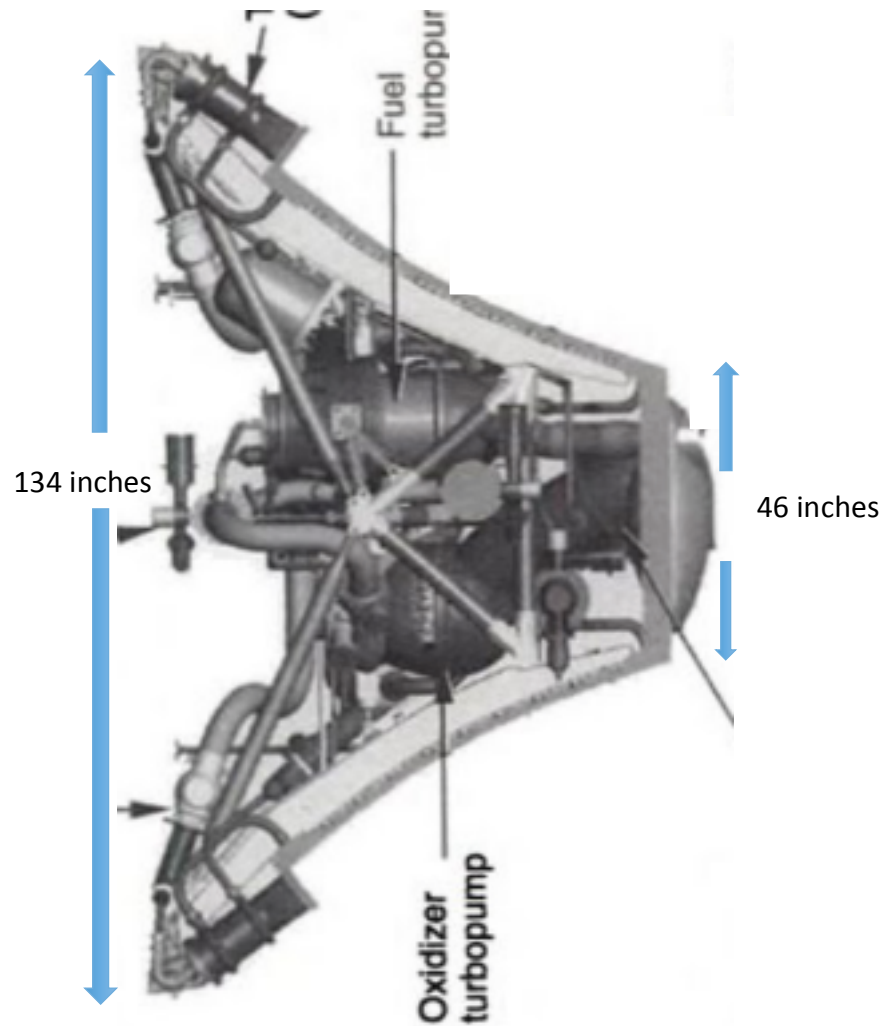
Figure 3.1.1.3.1 – XRS 2200 Linear Aerospike Illustration [11]

Protruding from the combustion chambers on the cowling, the initial nozzles of the Aerospike accelerates the flow up to Mach 2.5, the AR of these nozzles are 3.05. The overall effective AR of this Linear Aerospike is 58. Meaning, when the outer jet boundary is parallel with the rockets velocity vector, the throat area to plume exit AR is 58. With the forty percent truncation of the spike, the overall length of the nozzle only reaches 80 inches long [18].

Not all the dimensions of every element for the XRS-2200 nozzle are not known, thus geometry similar to the actual dimensions are used. For the geometry used in the study, the dimensions are summarized in the Table 1 below. The early nozzle section was generated based on a known nozzle geometry that produced successful results, as shown in Figure 3.1.1.3.3 and Figure 3.1.1.3.4.

Table 3.1.1.3.1 – Summary of the geometry details

Dimensions and Parameters	Data
Base width:	46 inches
Top end width	133 inches
Height ramp	79 inches
AR initial nozzles	1.5
AR*	60
θ	30 degrees
Control volume length:	348 inches
Control volume width:	174 inches

Ramp developed using code detailed in the Appendices of this study
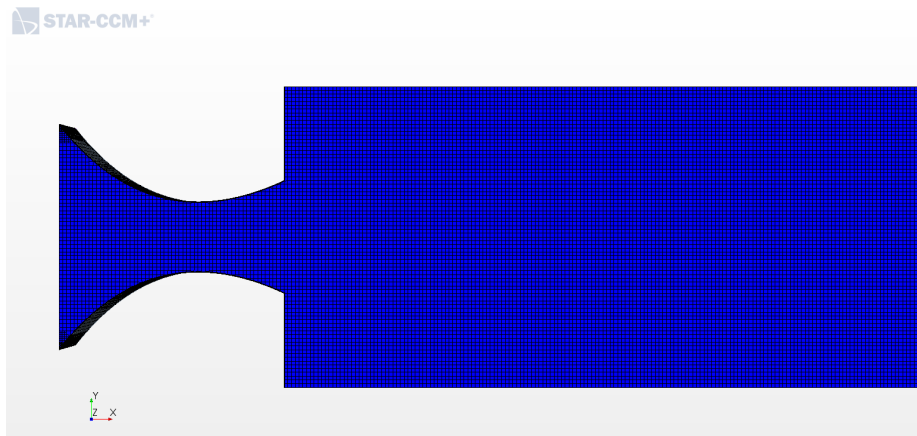
Figure 3.1.1.3.2 - Early Expansion & Injection Nozzle 2D Mesh
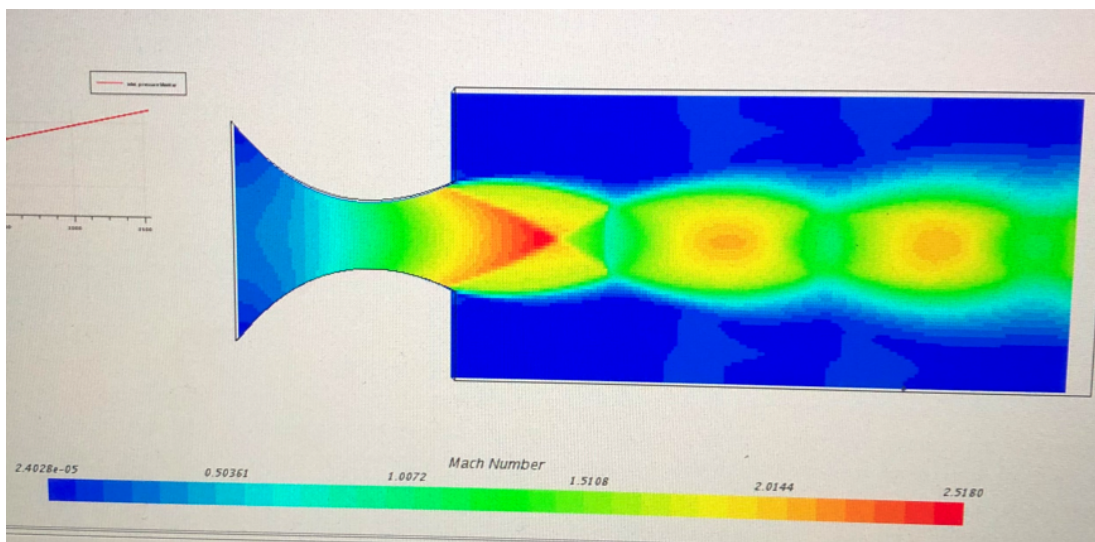
Figure 3.1.1.3.3 – Early Expansion & Injection Nozzle Test Simulation
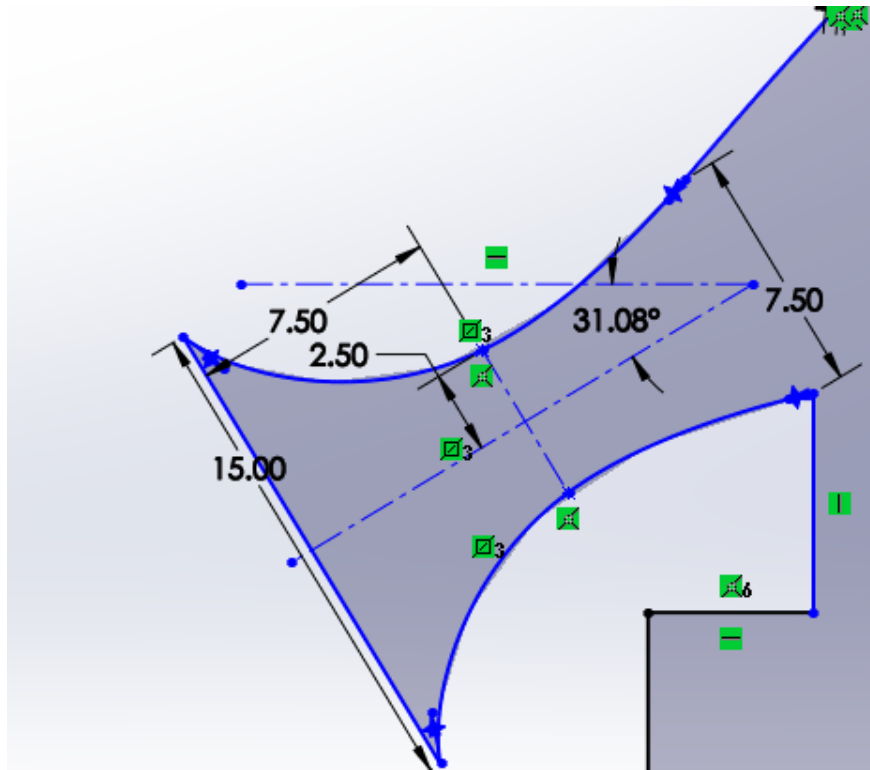
Figure 3.1.1.3.4 - Early Expansion Nozzle Dimension (inches)
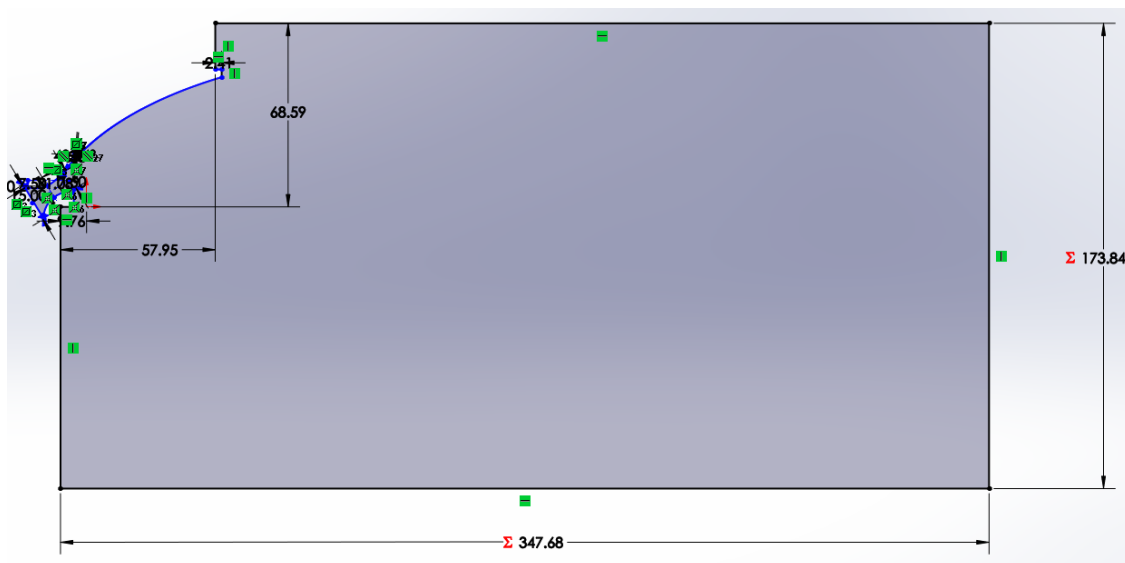
Figure 3.1.1.3.5 - Cross section of the control volume.

Above in Figure 3.1.1.3.3 and Figure 3.1.1.3.4, the nozzle used in the main initial nozzle and the secondary nozzle responsible for injecting fluid is tested. The goal of this nozzle test is to discover the optimal pressure in the inlet of the convergent section of the nozzle. As the pressure in the nozzle inlet increased the accelerating through the divergent section accelerated. The resulting mesh and test simulation for the convergent divergent nozzle shows similarity to the real initial expansion nozzle of XRS-2200 Linear Aerospike. One such metric was Mach number of the exit flow, which was between Mach 1.8 and Mach 2.5.

3.1.2   Injector Geometry

3.1.2.1   Nozzle

The injection nozzle for the film-cooling will be modeled as a simple convergent-divergent (C-D) nozzle. The geometry will be identical to main C-D nozzle, except for the throat being smaller. The area ratio is 1.5, which is identical to the main nozzle, however the exit diameter is reduced to 3 inches. Ensuring the velocity of the fluid is subsonic, the pressure in the chamber of the injection nozzle will be varied between 200,000-750,000 Pa. Exploring what pressure might yield a shockwave in the flow, the pressure in the inlet of the injection nozzle will be increased to 1,000,000 Pa. The fluid will inject into the flow at a 40 degree angle with respect to the localized normal as depicted in Figure 3.1.2.1.1.
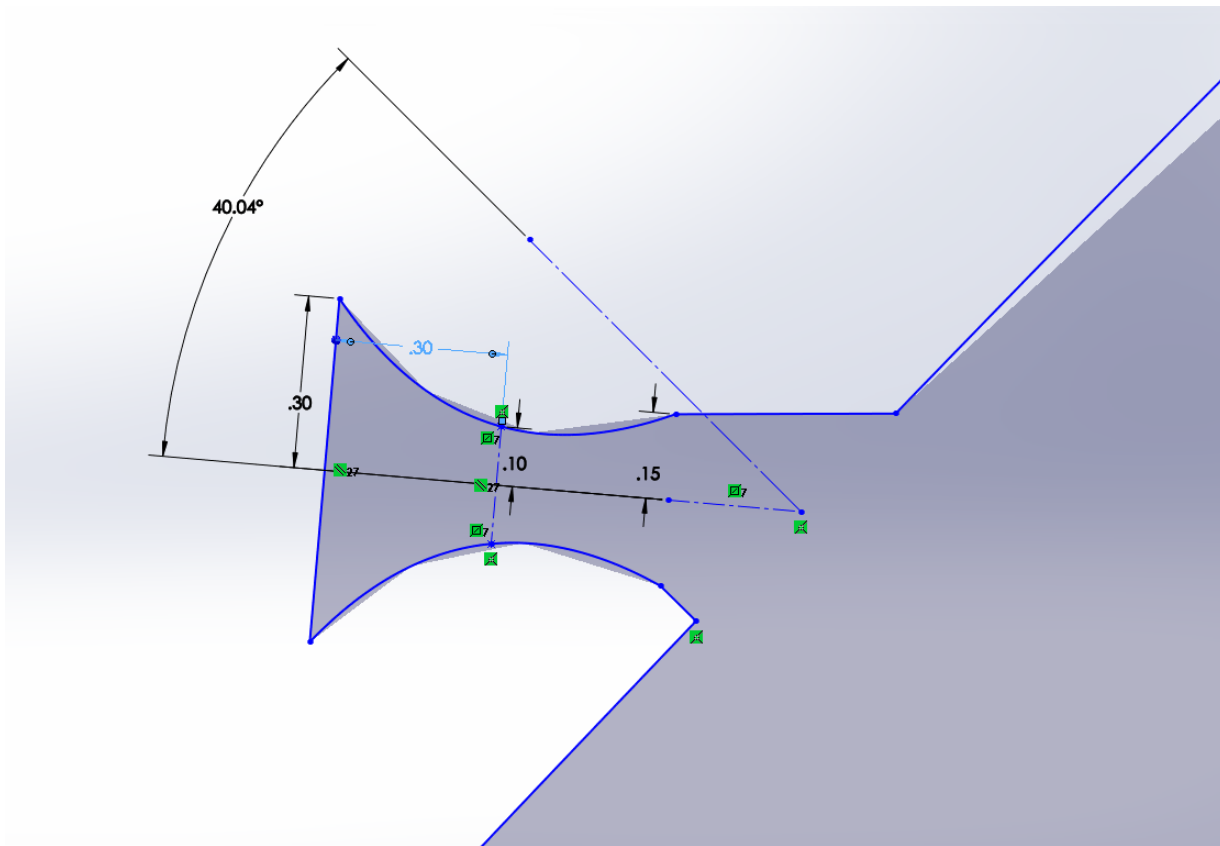
Figure 3.1.2.1.1 – Injection Nozzle Dimension (units: inches)

For the scope of this analysis, a singular injection nozzle will be placed just outside the nozzle on the expansion ramp. This singular injection will be a base line for the injection flow analysis; mainly because increasing the number of flow injectors will either increase the mass flow rate or decrease the injection flow velocity.

The injector diameter will be set at 1.5 inch. The size of this injector is selected as an arbitrary size. Ultimately, if the film-cooling proves to be beneficial with arbitrary sized injector, then a piece of future work will be to determine the optimized size of the injector(s).

3.2   Governing Equations

There are three main equations that govern fluid dynamics. They are continuity, momentum, and energy. Behind the user interface of the CFD software programs, these three fundamental equations work to simulate how the fluid would interact with boundaries and bodies in the flow. Fluids, unlike ridged bodies, are more malleable and are greatly changed from influence of the surrounding environment.

With ridged bodies, the velocity or acceleration of the body is uniform for every particle that makes up that body. This makes applying the fundamental physics principles such as Newton's second law of motion and energy conservation equations straightforward.

However, with fluids, the velocity or acceleration may be different for every particle in the flow, adding another level of complexity to the analysis. Navigating this complexity, the flow needs to be broken down in to smaller more manageable segments or elements called control volumes.

The finite control volume (CV) defines a small region in the flow where fluid may enter and exit. These volumes provide a means to apply the fundamental physics principles with known dimensions where volume and surface integrals or second order partial differential equations can be applied. These are known as the conservation governing equations. The details of these equations are in the subsequent sections.

3.2.1   Continuity

The basic mass conservation continuity equation is density of the fluid, times the velocity of the flow, times the cross sectional area of the control volume where the flow enters. This expression details that mass is conserved inside the control volume. The surface integral describes the summation of fluid particles flowing into and out of the control volume. This influx of fluid occurs when the surface area vector, ds, pointing in the opposite direction of the flow velocity. The exodus of fluid occur when the surface area vector, ds, pointing in the same direction of the flow velocity. Vector diagram in Figure 3.2.1.1 illustrates the fluid interaction with the CV. Equation (3.2.1.1) describes the mathematical representation of the flux described above.
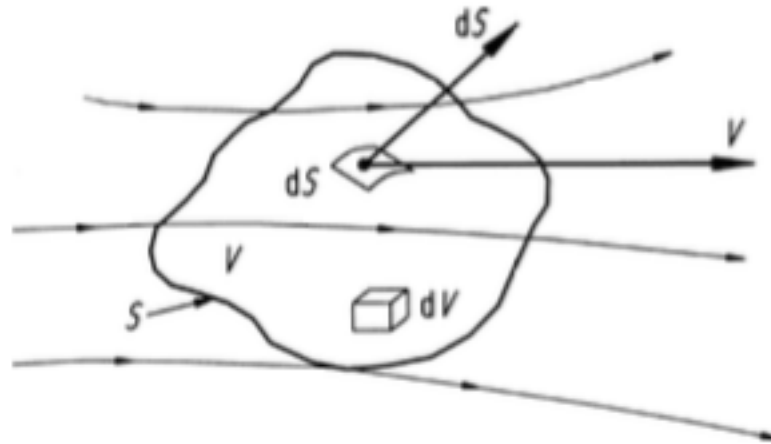
Figure 3.2.1.1 – Control volume illustration [19]

From Anderson's textbook, the following derivation for the conservative form of the continuity equation for a control volume fixed in space is as follows.

Net mass flow out of control volume = Time rate decrease of mass in the control volume

Looking at the left side of the equation.

$$\rho V_n ds = \rho \vec{V} \cdot \vec{ds}$$

Integrating over the surface obtains.

$$\text{Net mass flow out of control volume} = \oiint \rho \vec{V} \cdot \vec{ds} \tag{3.2.1.1}$$

Now, evaluating the right side of the equation.

$$\text{total mass in the control volume} = \oiiint \rho \, d\forall$$

Where $d\forall$ is the elemental volume, denoted by dV in the Figure 3.2.1.1 above. Then taking the derivative yields the time rate of mass change in the control volume. Adding a negative sign denotes a decrease in mass, as shown in the Equation (3.2.1.2) below.

$$\text{Time rate decrease of mass in the control volume} = -\frac{\partial}{\partial t}\oiiint \rho \, d\forall \tag{3.2.1.2}$$

Then combining Equation (3.2.1.1) and (3.2.1.2) respectively in the above expression and manipulating the form, produces the conservative integral form of the continuity equation, Equation (3.2.1.3), for a control volume fixed in space.

$$\oiint \rho \vec{V} \cdot \vec{ds} = -\frac{\partial}{\partial t} \iiint \rho \, d\forall$$

$$\frac{\partial}{\partial t} \iiint \rho \, d\forall + \oiint \rho \vec{V} \cdot \vec{ds} = 0 \qquad\qquad (3.2.1.3)$$

From the limits of integration, this form can be written as the following.

$$\iiint \rho \frac{\partial}{\partial t} d\forall + \oiint \rho \vec{V} \cdot \vec{ds} = 0$$

$$\oiint \rho \vec{V} \cdot \vec{ds} = \iiint \nabla \cdot (\rho \vec{V}) d\forall = 0$$

Thus, the equation becomes.

$$\iiint \frac{\partial \rho}{\partial t} d\forall + \iiint \nabla \cdot (\rho \vec{V}) d\forall = 0$$

$$\iiint [\frac{\partial \rho}{\partial t} + \nabla \cdot (\rho \vec{V})] d\forall = 0$$

Due to the arbitrary nature of the control volume, the only way the statement can be true is if the integrand is equal to zero Equation (3.2.1.4)

$$\frac{\partial \rho}{\partial t} + \nabla \cdot (\rho \vec{V}) = 0 \qquad\qquad (3.2.1.4)$$

Resulting in the conservative differential form of the continuity equation [19]. For the study, this will be the case, the CV will be fixed in space and fluid will enter via the defined inlets and exit through the outlets.

3.2.2   Momentum Navier-Stokes

At the root of the Navier-Stokes equations is Newton's second law of motion, the famous force equals mass times acceleration. The force side of the equation is comprised of two types of forces body and surface experienced by the fluid element. Body forces act directly on the volumetric mass of the fluid. These forces act on the body without physical contact, examples include gravitational, electrical, and magnetic forces.

The other type of forces, surface forces or viscous forces, acts directly on the fluid element, shown below in Figure 3.2.2.1. These forces are by products of other fluid element interactions. One source is pressure distribution acting normal to the fluid element from adjacent fluid. Another way of describing this sources is the time rate of change of volume of the fluid element. The other source is stress acting on the surfaces of the element caused by adjacent fluid elements sliding parallel to one another. These elements produce tugging or shear stress on the adjacent elements as they move in space.

Another way of describing this source is the time rate of change of deformation of the fluid element. The combination of these forces can be seen in the high level derivation detailed below.

$$\text{Net body forces in the x-direction} = \rho f_x(dx, dy, dz)$$

$$
\begin{aligned}
\text{Net surface forces in the x-direction} = {} & \left[p - \left(p + \frac{\partial p}{\partial x}dx\right)\right]dydz + \left[\left(\tau_{xx} + \frac{\partial \tau_{xx}}{\partial x}dx\right) - \tau_{xx}\right]dydz \\
& + \left[\left(\tau_{yx} + \frac{\partial \tau_{yx}}{\partial y}dy\right) - \tau_{yx}\right]dxdz \\
& + \left[\left(\tau_{zx} + \frac{\partial \tau_{zx}}{\partial z}dz\right) - \tau_{zx}\right]dxdy
\end{aligned}
$$
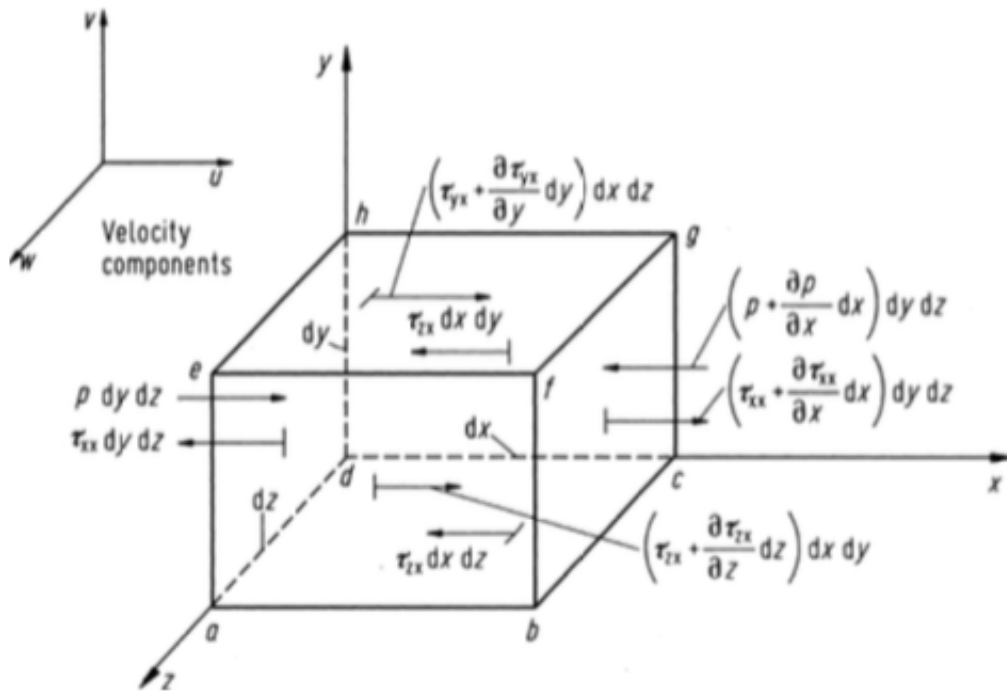
Figure 3.2.2.1 – Diagram of fluid forces experienced by a control volume [19].

From Anderson's textbook, the following derivation for the momentum and Navier-Stokes equation for a CV fixed in space is as follows. Looking along one axis as depicted in Figure 3.2.2.1, we get the following in Equation (3.2.2.1).

$$F = Ma \tag{3.2.2.1}$$

The total force experienced by the fluid element along a single axis, x direction is the algebraic sum of the above expressions. The result is as follows.

$$F_x = \sum Forces\ in\ x\ axis\ direction$$

$$F_x = F_{Surface} + F_{Body}$$

$$F_x = \left[-\frac{\partial p}{\partial x} + \frac{\partial \tau_{xx}}{\partial x} + \frac{\partial \tau_{yx}}{\partial y} + \frac{\partial \tau_{zx}}{\partial z} \right] dxdydz + \rho f_x(dx,dy,dz) \tag{3.2.2.2}$$

After obtaining the force component of Newton's law in differential form Equation (3.2.2.2), the mass and acceleration terms must be expressed in similar terms. Recall that volume as a whole is defined as having dimensional components in the xyz-directions. Breaking this volume in to infinitesimal elements this becomes dxdydz, as seen in Equation (3.2.2.3) below.

$$Mass = \rho V$$

$$Mass = \rho\ dxdydz \tag{3.2.2.3}$$

The acceleration of the fluid element is the time rate of change of the velocity of said fluid element. In differential terms the acceleration in the x-direction is described Equation (3.2.2.4) as follows.

$$a_x = \frac{Du}{Dt} \tag{3.2.2.4}$$

Gathering all the expressions for F, M, and a, and plugging in Equations (3.2.2.2), (3.2.2.3), and (3.2.2.4) into Equation (3.2.2.11) results in Equation (3.2.2.5)

$$\rho \frac{Du}{Dt} = \left[-\frac{\partial p}{\partial x} + \frac{\partial \tau_{xx}}{\partial x} + \frac{\partial \tau_{yx}}{\partial y} + \frac{\partial \tau_{zx}}{\partial z} \right] + \rho f_x \tag{3.2.2.5}$$

The differential form of the force equation for the x-axis direction. Similarly, the force equation for the y and z-axis are as follows in Equation (3.2.2.6) and (3.2.2.7)

$$\rho \frac{Dv}{Dt} = \left[-\frac{\partial p}{\partial y} + \frac{\partial \tau_{xy}}{\partial x} + \frac{\partial \tau_{yy}}{\partial y} + \frac{\partial \tau_{zy}}{\partial z} \right] + \rho f_y \tag{3.2.2.6}$$

$$\rho \frac{Dw}{Dt} = \left[-\frac{\partial p}{\partial z} + \frac{\partial \tau_{xz}}{\partial x} + \frac{\partial \tau_{yz}}{\partial y} + \frac{\partial \tau_{zz}}{\partial z} \right] + \rho f_z \tag{3.2.2.7}$$

The left side of the above equations, when substituted into the Substantial Derivative equation, Equation (3.2.2.8), yields the famed Navier-Stokes equations, Equation (3.2.2.9), (3.2.2.10) and (3.2.2.11).

$$\text{Substantial Derivitive: } \rho \frac{Du}{Dt} = \frac{\partial(\rho u)}{\partial t} + \nabla \cdot (\rho u \vec{V}) \qquad (3.2.2.8)$$

$$x \text{ direction}: \quad \frac{\partial(\rho u)}{\partial t} + \nabla \cdot (\rho u \vec{V}) = \left[-\frac{\partial p}{\partial x} + \frac{\partial \tau_{xx}}{\partial x} + \frac{\partial \tau_{yx}}{\partial y} + \frac{\partial \tau_{zx}}{\partial z}\right] + \rho f_x \qquad (3.2.2.9)$$

$$y \text{ direction}: \quad \frac{\partial(\rho v)}{\partial t} + \nabla \cdot (\rho v \vec{V}) = \left[-\frac{\partial p}{\partial y} + \frac{\partial \tau_{xy}}{\partial x} + \frac{\partial \tau_{yy}}{\partial y} + \frac{\partial \tau_{zy}}{\partial z}\right] + \rho f_y \qquad (3.2.2.10)$$

$$z \text{ direction}: \quad \frac{\partial(\rho w)}{\partial t} + \nabla \cdot (\rho w \vec{V}) = \left[-\frac{\partial p}{\partial z} + \frac{\partial \tau_{xz}}{\partial x} + \frac{\partial \tau_{yz}}{\partial y} + \frac{\partial \tau_{zz}}{\partial z}\right] + \rho f_z \qquad (3.2.2.11)$$

For the integration of viscous fluid effects, include the expanded equations for the shear stress terms. These terms are known as time rate of strain or velocity gradients and can be applied to fluids that fall under the classification of Newtonian.

$$\tau_{xx} = \lambda \nabla \cdot \vec{V} + 2\mu \frac{\partial u}{\partial x}$$

$$\tau_{yy} = \lambda \nabla \cdot \vec{V} + 2\mu \frac{\partial v}{\partial y}$$

$$\tau_{zz} = \lambda \nabla \cdot \vec{V} + 2\mu \frac{\partial w}{\partial z}$$

$$\tau_{xy} = \tau_{yx} = \mu\left(\frac{\partial v}{\partial x} + \frac{\partial u}{\partial y}\right)$$

$$\tau_{xz} = \tau_{zx} = \mu\left(\frac{\partial u}{\partial z} + \frac{\partial w}{\partial x}\right)$$

$$\tau_{yz} = \tau_{zy} = \mu\left(\frac{\partial w}{\partial y} + \frac{\partial v}{\partial z}\right)$$

$$\lambda = -\frac{2}{3}\mu$$

The result, complete conservative Navier-Stokes equations, Equation (3.2.2.12), (3.2.2.13), and (3.2.2.14) for fluid dynamics

$$\frac{\partial(\rho u)}{\partial t} + \frac{\partial(\rho u^2)}{\partial x} + \frac{\partial(\rho uv)}{\partial y} + \frac{\partial(\rho uw)}{\partial z}$$
$$= -\frac{\partial p}{\partial x} + \frac{\partial}{\partial x}\left(\lambda \nabla \cdot \vec{V} + 2\mu \frac{\partial u}{\partial x}\right) + \frac{\partial}{\partial y}\left(\mu\left(\frac{\partial v}{\partial x} + \frac{\partial u}{\partial y}\right)\right) + \frac{\partial}{\partial z}\left(\mu\left(\frac{\partial u}{\partial z} + \frac{\partial w}{\partial x}\right)\right)$$
$$+ \rho f_x \qquad (3.2.2.12)$$

$$\frac{\partial(\rho v)}{\partial t} + \frac{\partial(\rho uv)}{\partial x} + \frac{\partial(\rho v^2)}{\partial y} + \frac{\partial(\rho vw)}{\partial z}$$
$$= -\frac{\partial p}{\partial y} + \frac{\partial}{\partial x}\left(\mu\left(\frac{\partial v}{\partial x} + \frac{\partial u}{\partial y}\right)\right) + \frac{\partial}{\partial y}\left(\lambda \nabla \cdot \vec{V} + 2\mu \frac{\partial v}{\partial y}\right) + \frac{\partial}{\partial z}\left(\mu\left(\frac{\partial w}{\partial y} + \frac{\partial v}{\partial z}\right)\right) + \rho f_y \qquad (3.2.2.13)$$

$$\frac{\partial(\rho w)}{\partial t} + \frac{\partial(\rho w u)}{\partial x} + \frac{\partial(\rho w v)}{\partial y} + \frac{\partial(\rho w^2)}{\partial z}$$

$$= -\frac{\partial p}{\partial z} + \frac{\partial}{\partial x}\left(\mu(\frac{\partial u}{\partial z} + \frac{\partial w}{\partial x})\right) + \frac{\partial}{\partial y}\left(\mu(\frac{\partial w}{\partial y} + \frac{\partial v}{\partial z})\right) + \frac{\partial}{\partial z}\left(\lambda\nabla\cdot\vec{V} + 2\mu\frac{\partial w}{\partial z}\right) + \rho f_z$$

(3.2.2.14)

[19]

3.2.3 Energy

The energy governing equations are constructed from the fundamental principle that energy cannot be created nor destroyed. The first law of thermodynamics is energy conservation; energy can be converted from one form to another, between mechanical, electrical, or chemical in the form of kinetic, potential, and vibrational. Qualitatively, energy conservation is rate of change inside the fluid element is equal to the net heat flux into the fluid plus the work done on the element due to external forces.
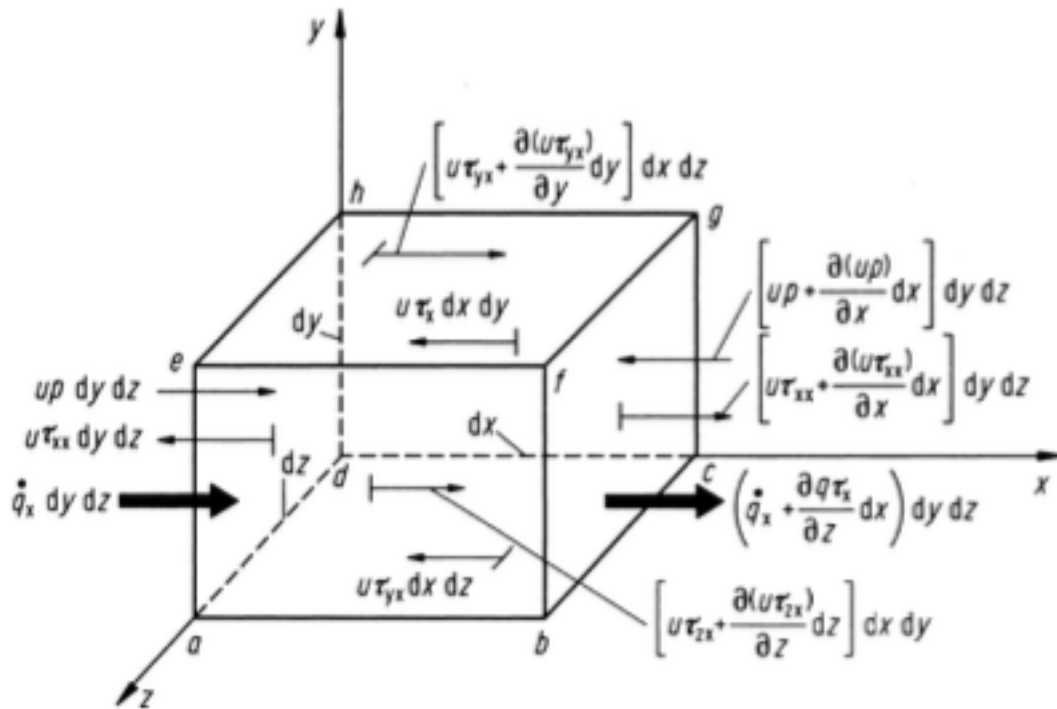
Figure 3.2.3.1 – Diagram of fluid forces experienced by a control volume [19].

Rate of energy change inside the fluid element	=	Net flux of heat into the fluid element	+	Rate of work done on the element due to body and surface forces

Evaluating the left side of the equation, the time rate of change of energy inside the fluid element is equal to the sum of the internal energy and kinetic energy. Evaluating these two components on a per unit mass basis, and using a form of Equation (3.2.2.8) produces

Rate of energy change inside the fluid element： $\rho \dfrac{D}{Dt}\left(e_{energy}+\dfrac{V^2}{2}\right)dxdydz$ (3.2.3.1)

Addressing the right side of the equation, expressions for net flux of heat into the element and work done on the fluid by the surrounding fluid elements. The heat flux component has two sub components that contribute to overall heating, volumetric and thermal conductive heating in the fluid element. Radiation entering into and exiting from the fluid is the cause of volumetric heating. Whereas temperature gradients across the fluid element boundary inducing conductive heat exchange

Volumetric heating of the element： $\rho\dot{q}dxdydz$

thermal conductive heating of the element： $-\left(\dfrac{\partial\dot{q}_x}{\partial x}+\dfrac{\partial\dot{q}_y}{\partial y}+\dfrac{\partial\dot{q}_z}{\partial z}\right)dxdydz$

Combining these two expressions for heat flux results in the following equation.

Net flux of heat in the fluid element： $\left(\rho\dot{q}-\dfrac{\partial\dot{q}_x}{\partial x}+\dfrac{\partial\dot{q}_y}{\partial y}+\dfrac{\partial\dot{q}_z}{\partial z}\right)dxdydz$

Net flux of heat in the fluid element： $\dot{q}_x=-k\dfrac{\partial T}{\partial x}$

Net flux of heat in the fluid element： $\left(\rho\dot{q}-\left(\dfrac{\partial\dot{q}_x}{\partial x}+\dfrac{\partial\dot{q}_y}{\partial y}+\dfrac{\partial\dot{q}_z}{\partial z}\right)\right)dxdydz$ (3.2.3.2)

The final term that remains to be defined is the expression for work done on the fluid. The forces responsible for doing work on the fluid element are the aforementioned body and surface forces. Fundamentally the work is defined as the dot product of the force vector and the velocity vector or the product of each axis component. Therefore, the expression for body forces is shown in Equation (3.2.3.1) and the surface forces in the x-direction are shown in Equation (3.2.3.2).

body force component of work done on fluid element： $\rho\vec{f}\cdot\vec{V}(dxdydz)$ (3.2.3.3)

surface force component of work done on fluid element in the x direction

： $\left(-\dfrac{\partial(up)}{\partial x}+\dfrac{\partial(u\tau_{xx})}{\partial x}+\dfrac{\partial(u\tau_{yx})}{\partial y}+\dfrac{\partial(u\tau_{zx})}{\partial z}\right)dxdydz$ (3.2.3.4)

Combining these two expressions for pressure and shear forces, the full equation for the work done can be constructed.

$$\left(-\left(\frac{\partial(up)}{\partial x}+\frac{\partial(vp)}{\partial y}+\frac{\partial(wp)}{\partial z}\right)+\frac{\partial(u\tau_{xx})}{\partial x}+\frac{\partial(u\tau_{yx})}{\partial y}+\frac{\partial(u\tau_{zx})}{\partial z}+\frac{\partial(v\tau_{xy})}{\partial x}+\frac{\partial(v\tau_{yy})}{\partial y}+\frac{\partial(v\tau_{zy})}{\partial z}+\frac{\partial(w\tau_{xz})}{\partial x}\right.$$
$$\left.+\frac{\partial(w\tau_{yz})}{\partial y}+\frac{\partial(w\tau_{zz})}{\partial z}\right)dxdydz+\rho\vec{f}\cdot\vec{V}(dxdydz)$$

Substituting Equation (3.2.3.1), (3.2.3.2), (3.2.3.3), and (3.2.3.4) into the expression for energy aforementioned yield the conservative form of the energy equation, Equation (3.2.3.5).

$$\rho\frac{D}{Dt}\left(e_{energy}+\frac{V^2}{2}\right) \tag{3.2.3.5}$$
$$=\rho\dot{q}+\frac{\partial}{\partial x}\left(k\frac{\partial T}{\partial x}\right)+\frac{\partial}{\partial y}\left(k\frac{\partial T}{\partial y}\right)+\frac{\partial}{\partial z}\left(k\frac{\partial T}{\partial z}\right)-\frac{\partial(up)}{\partial x}-\frac{\partial(vp)}{\partial y}-\frac{\partial(wp)}{\partial z}$$
$$+\frac{\partial(u\tau_{xx})}{\partial x}+\frac{\partial(u\tau_{yx})}{\partial y}+\frac{\partial(u\tau_{zx})}{\partial z}+\frac{\partial(v\tau_{xy})}{\partial x}+\frac{\partial(v\tau_{yy})}{\partial y}+\frac{\partial(v\tau_{zy})}{\partial z}+\frac{\partial(w\tau_{xz})}{\partial x}$$
$$+\frac{\partial(w\tau_{yz})}{\partial y}+\frac{\partial(w\tau_{zz})}{\partial z}+\rho\vec{f}\cdot\vec{V}$$

[19]

3.3 CFD Mesh Strategy

3.3.1 Mesh Density

The base size of the mesh is set at 0.75 inches. A mesh that is 200 percent of the base size is utilized in areas where flow is not changing velocity or direction or does not interact with a boundary of the control volume. In areas of interest, near the main and injection nozzles and the expansion ramp wall, a higher mesh density was employed to best capture flow phenomena and fluid interactions. Near these surfaces, the prism layer parameters dictate the increase in mesh density near the nozzles and the expansion ramp.

3.3.2 Mesh Type

A quadrilateral mesh will be employed in the computational space around the truncated spike. In the region near the expansion ramp, a fine mesh will be constructed to capture the fluid interaction between the flow on the ramp and the injection flow. Capturing the velocity gradient in the boundary layer of the expanding flow, a prism layer will be employed to capture fluid interactions near the body.
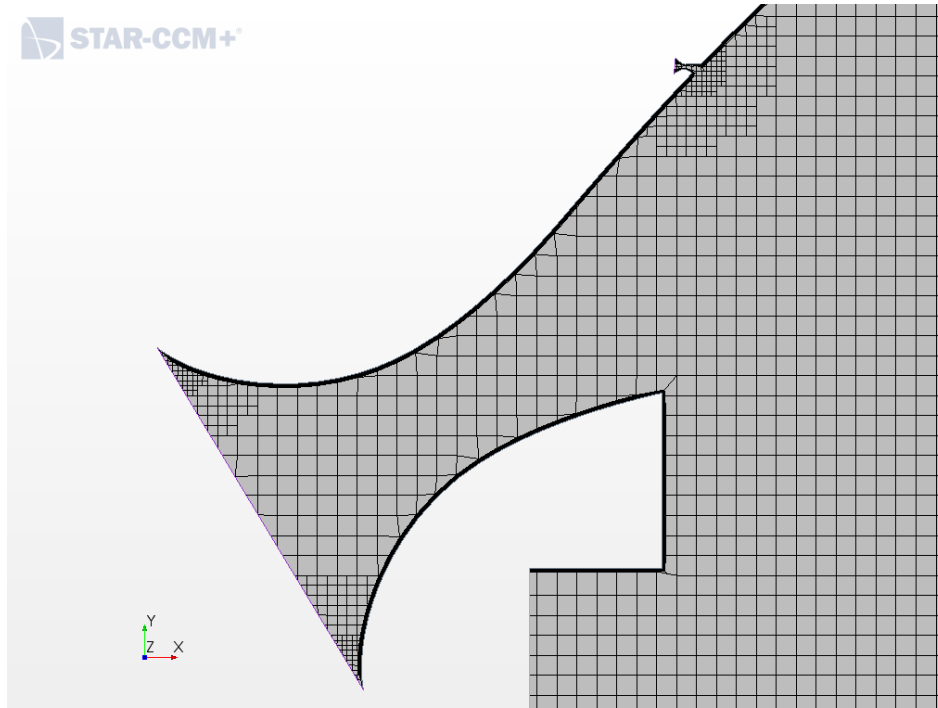
Figure 3.3.2.1 – 2D Mesh of Main Nozzle

3.3.3   Mesh Details

The 2D mesh employed by the CFD program utilizes 118,000 cells to perform the computation. The simulation domain is derived from a volume mesh that contains 1.2 million cells. When the number of cells increases, the computational time increases proportionally. Below in Table 3.3.3.1 detail the mesh properties for used in the study. Figure 3.3.3.1 illustrates the finalized meshed geometry used for the study.

Table 3.3.3.1 - Mesh Control Parameters

Parameters	Value
Base Size	0.75 inches
Maximum cell size	200%
Number of prism layers	15
Prism layer stretch ratio	1.2
Prism layer thickness	20 Percent
Mesh growth rate	Medium
Volume mesh cell count	1,200,000
2D mesh cell count	118,000
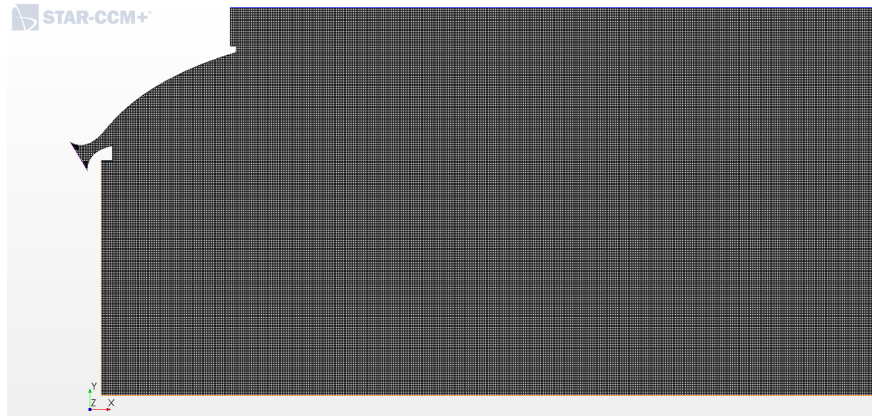
Figure 3.3.3.1– 2D Mesh of Simulation Environment

3.3.4   Mesh Refinement

A point of diminishing returns is reached when over 1,000,000 cells are employed. Cell quantities greater than this will only slow down simulation times without improving the accuracy of the results. Based on the processing capabilities of the tools available, a volume mesh containing 1.2 million cells is pushing the limits of the computer. More cells would consume more processing power and decrease simulation speeds.

3.4   CFD Physics

3.4.1   Fluid

The gas composition used in the CFD solver is cold gas at standard temperature of 300k and pressure 101,325 Pa. The equation of state assumed for the fluid was ideal gas, meaning the fluid has a fixed value for the specific heat. The simulation assumes a constant value for gamma, being 1.4; this is a sufficient assumption for the scope of this study, since the thermal environment of the chamber will be neglected.

3.4.2.2 Injector Fluid

The gas expelled from both the injector and main nozzles are identical. Meaning, the value for gamma and the specific gas constant of the injected fluid will be uniform throughout the simulation environment. A divergent section would need to be present to accelerate the injection flow above sonic conditions. For the situation illustrated in this paper, the injection velocity will be adjusted based on chamber pressure conditions, which may exceed Mach 1.

Table 3.4.2.2 – The Conditions and Sonic Calculations for Ideal Gas

Parameters	Data
Gamma (γ)	1.4
Temperature	300k
Specific Gas Constant	28.013 j/kg-k

Speed of Sound	353.07 m/s
Injection velocity (1/4 sonic velocity)	88.26 m/s
Injection velocity (2/4 sonic velocity)	176.53 m/s
Injection velocity (3/4 sonic velocity)	264.80 m/s

3.4.2   CFD Regions Boundaries

3.4.2.1   Main Nozzle

The main nozzle is configured as a stagnation inlet with an initial total pressure set to a value that is much greater than the free-stream pressure. The face upstream of the convergent section of the nozzle throat was defined as the inlet and set at various total pressure values. During the initial development of the simulation, the solution would not converge and in most cases would encounter a float point error, which is non-recoverable. Attempts were made to solve the issue by adjusting the viscosity ratios and other fluid property ratios, which solved the issue.

However, this solution inadvertently created other issues with how the flow interacted with the expansion ramp. Another approach was to slowly ramp up the pressure at the stagnation inlet, speculating the float point error was due to the large pressure difference between the stagnation inlet and the free-stream conditions in the control volume. A small piece of code was implemented in the definition of the Stagnation inlet, gradually increasing the total pressure at the inlet by 1000 pa after each iteration. Figure 3.4.2.1.1 illustrates a graph showing the gradual increase in total pressure at the stagnation inlet.
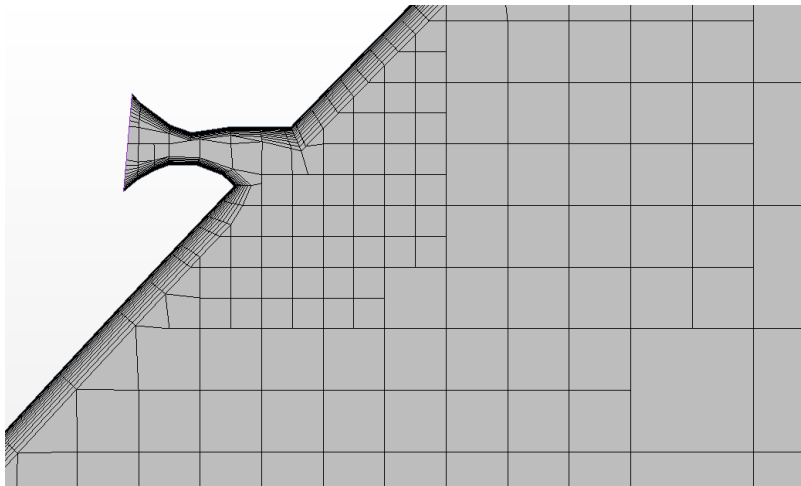
Figure 3.4.2.1.1 – 2D Mesh of Injection Nozzle

The solution was successful, solving the float point issue, ensuring the pressure in the inlet produces supersonic flow on the Aerospike ramp, and producing a solution that converges.

3.4.2.2   Injector Nozzle

The injection nozzle is also configured as a stagnation inlet with an initial total pressure set to a value that is much greater than the free-stream pressure. The face upstream of the convergent section of the nozzle throat was defined as the inlet. The total pressure value at this inlet is varied in three simulation cases as highlighted in Section 4.2. Like the main nozzle, during the initial development of the simulation, the solution would not converge and in most cases would encounter a float point error. Initiating the simulation with a large pressure differential between the free-stream and the injection nozzle would cause a divergence in the simulation.

A similar approach is employed to solve this problem. The simulation is initiated with the total pressure in the main nozzle slowly increasing with the total pressure in the injection nozzle initially being zero. Then after the establishment of flow from the main nozzle (Figure 3.4.2.1.1), the author manually begins entering pressure values for the injection nozzle inlet in increments of 10,000 pa.

This method of slowly increasing pressure was successful, solving the float point issue, ensuring the pressure in the inlet produces flow that impinged on the main flow on the Aerospike ramp, and producing a solution that converges.

3.4.2.3   Free-stream Conditions

In the free-stream flow around the Linear Aerospike, initial pressure, initial temperature, and initial fluid velocity are set at constant values to simulate low speed conditions during a launch sea level. The Mach number of the flow is set at 0.5. The pressure is set at 1 atm, or 101,325 pa and the static temperature is set constant at 300k. Setting the flow velocity to 0.5 was found to work best for the simulations success, when running the simulation with an initial flow velocity being zero, float point errors force the solution to diverge.

3.4.2.4   Pressure Outlets

The outlet is under the same conditions as the free-stream conditions, however the initial flow velocity will be set to be zero.

3.4.3   Fluid Physics Models and Solvers

The fluid solvers and physics models employed in the CFD solution below are as follows.

Table 3.4.3.1 – Summary of CFD Physics Models

Star CCM Physics Models	Selection
Time	Steady
Material	Gas
Flow	Coupled
Equation of State	Ideal Gas
Viscous Regime	Turbulent
Reynolds-Averaged Turbulence	K-Epsilon Turbulence

4.   **Nozzle Performance Analysis**

4.1 **CFD Benchmark Results**

The results presented in the following section are used as benchmarking data; the flow will be compared with previously published data. Mach number, temperature, pressure, and flow velocity are compared to previous studies mentioned in the previously published data section.

4.1.1   Nozzle Performance Flow Visualization
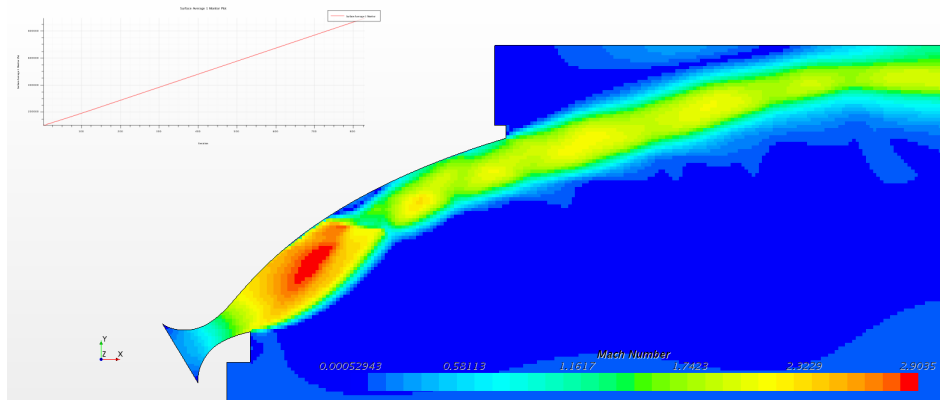
Figure 4.1.1.1 – Mach scene with increasing inlet pressure ramping up to 25 atm
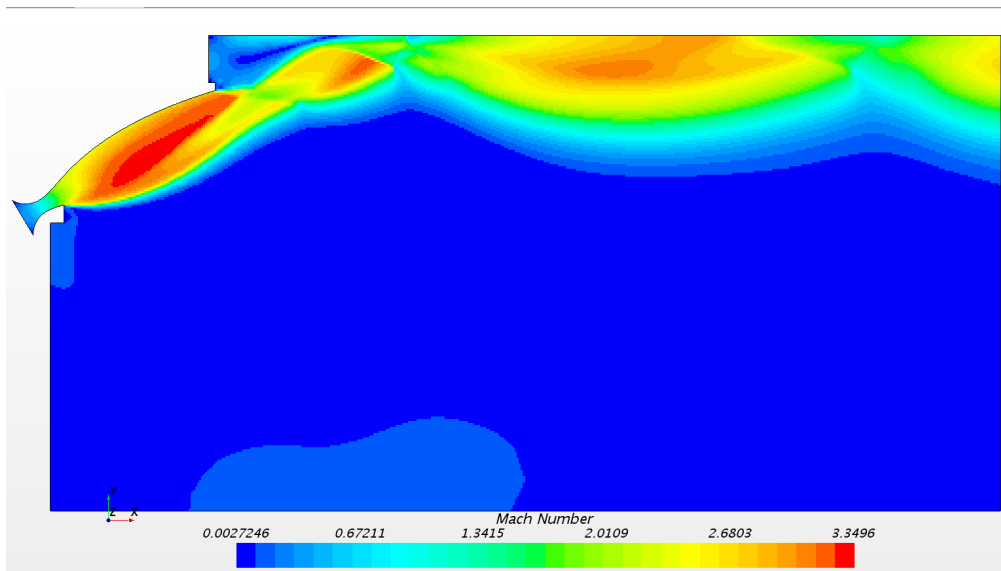
Figure 4.1.1.2 – Mach scene benchmark of Aerospike geometry
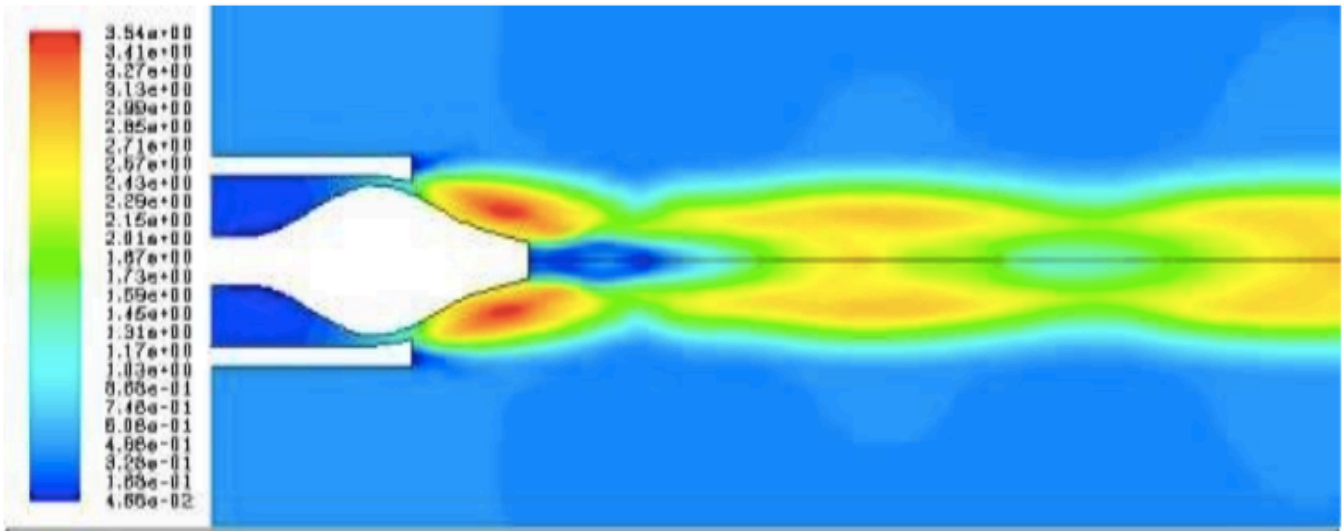
Figure 4.1.1.3 – Mach scene from Design Optimization of Aerospike Nozzle [15]

4.1.2   Temperature
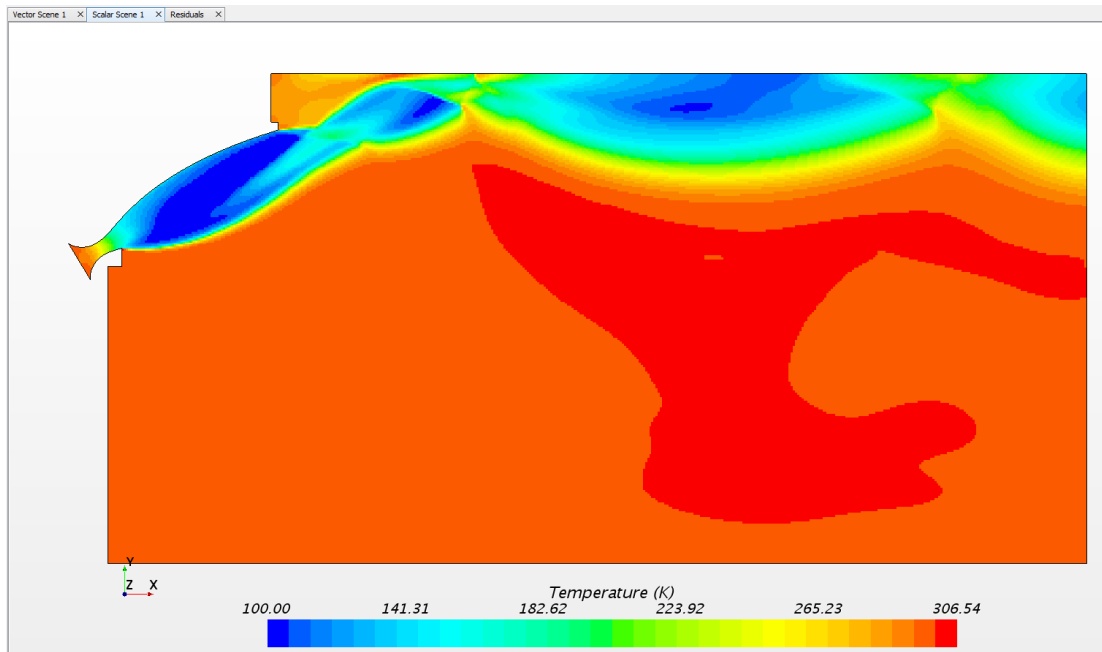
Figure 3.1.2.1 – Temperature scene benchmark of Aerospike geometry

4.1.3   Pressure
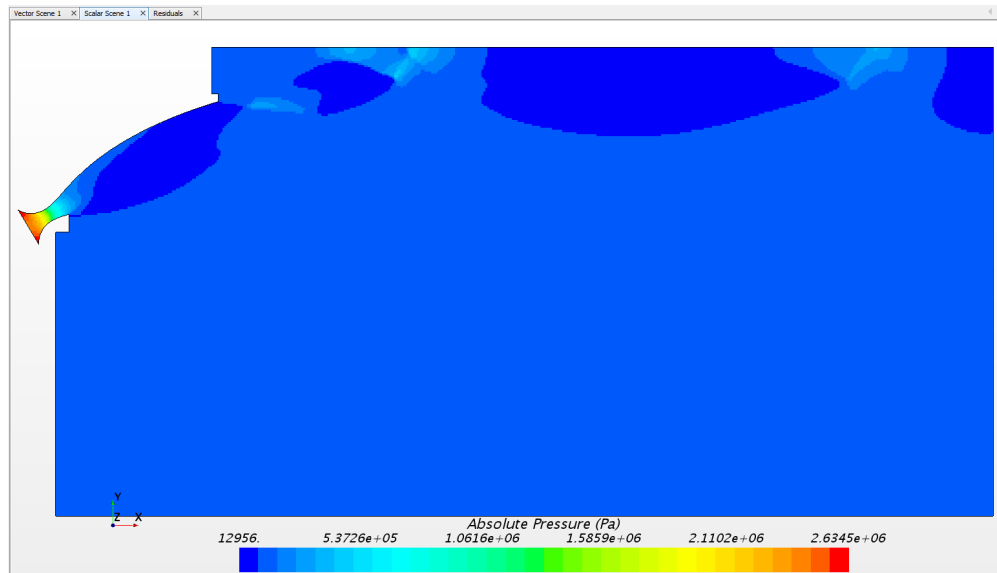
Figure 3.1.3.1 – Pressure scene benchmark of Aerospike geometry

4.1.4   Velocity Vector
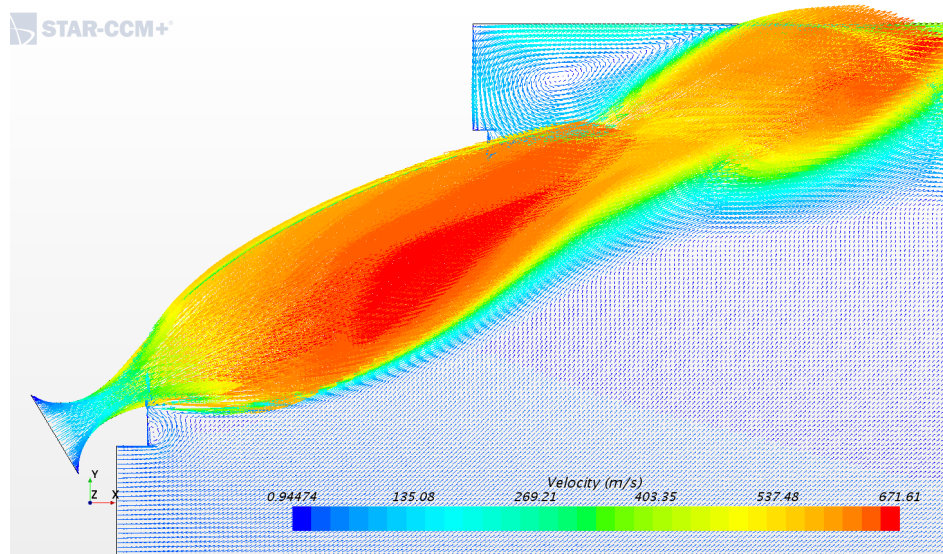
Figure 4.1.4.1 – Velocity vector scene benchmark of Aerospike geometry close up on nozzle

4.1.5 Extreme Case Nozzle Performance Flow Visualization
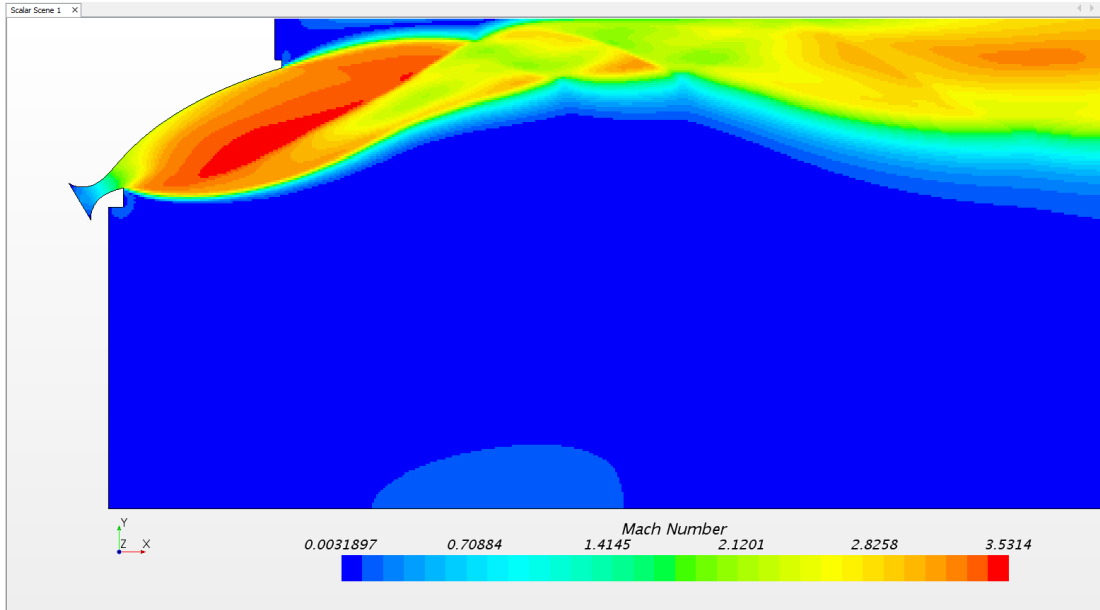
Figure 4.1.5.1 – Extreme case Mach scene benchmark of Aerospike geometry

4.1.6 Extreme Case Temperature
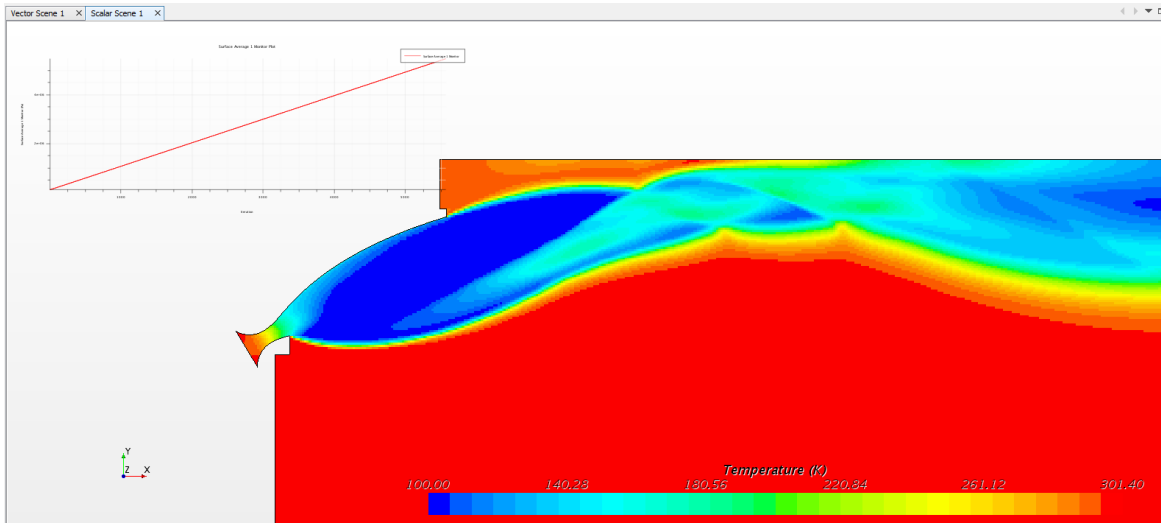
Figure 4.1.6.1 – Extreme case temperature scene benchmark of Aerospike geometry

4.1.7   Extreme Case Pressure
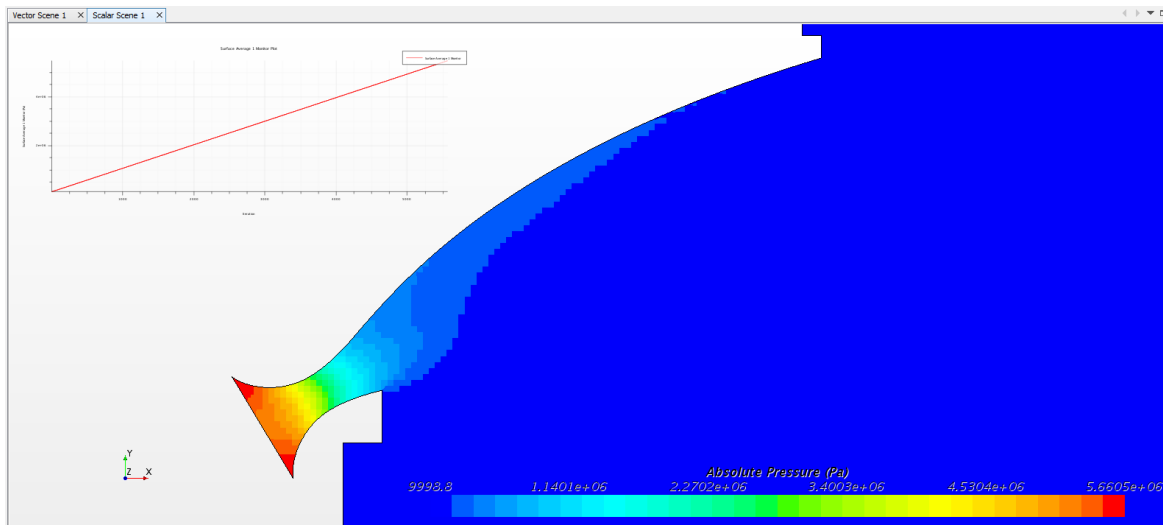
Figure 4.1.7.1 – Extreme case pressure scene benchmark of Aerospike geometry

4.1.8   Extreme Case Velocity Vector
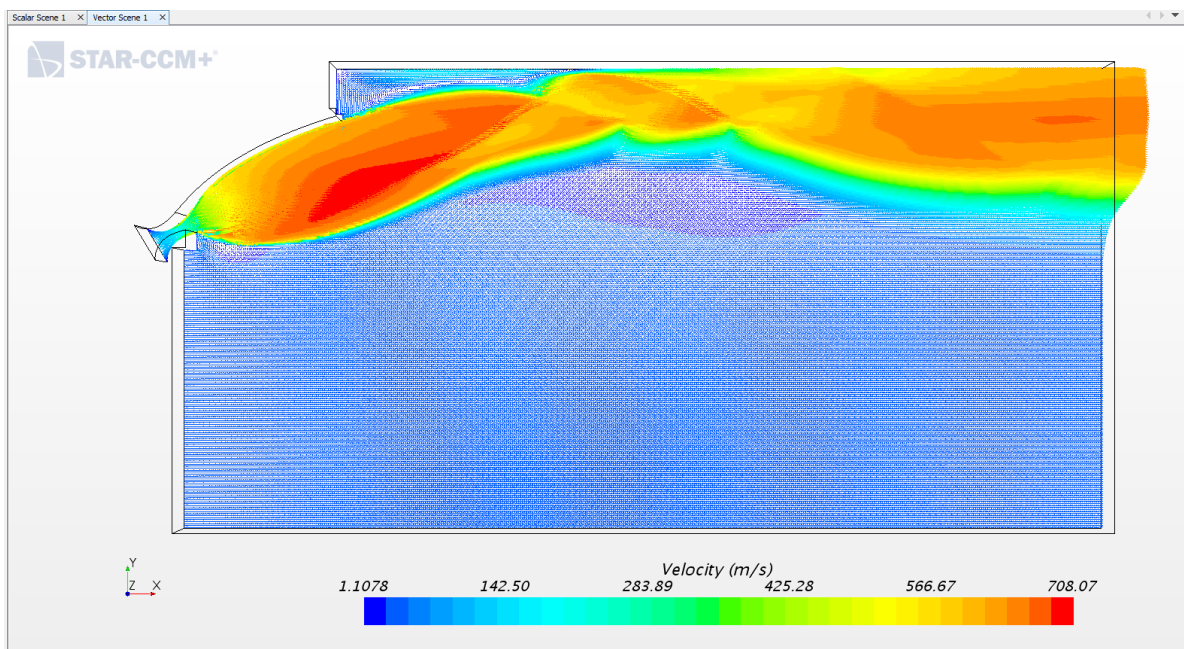
Figure 4.1.8.1 – Extreme case velocity vector scene benchmark of Aerospike geometry
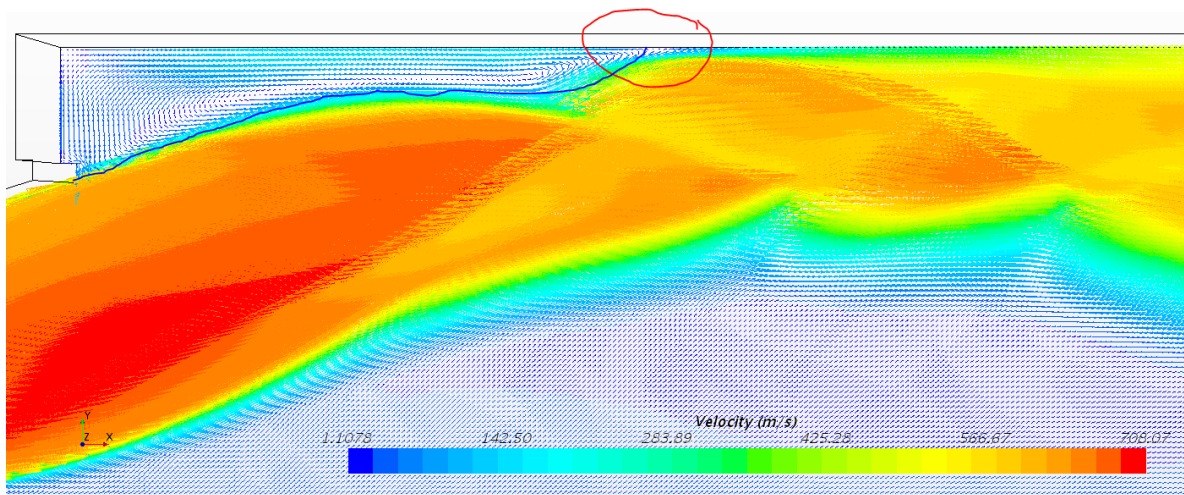
Figure 4.1.8.2 – Extreme case velocity vector scene with stagnation line tracing and point highlighted.

        The intent of Section 4.1 is to illustrate the similarities between previously published data on Aerospike flow simulations and the simulations produced for the purpose of this study. Performing a benchmark analysis is essential to the analytical process. Recreating a known simulation with similar geometry, allows for any performance improvements or hindrances to be attributed to the proposed alteration. As seen above the geometry created for this study matches that of a previous study, with only minor differences.

        The benchmark simulation results demonstrate that the Aerospike nozzle exhibits all of the same flow characteristics as previous studies. Using Figure 4.1.8.3 as a reference for flow characteristics, the outer jet boundary, region of recirculating flow, envelop shock region, stagnation line and point, and trailing shock are all present in the benchmark simulation results. Not only do these Aerospike flow elements exist, they form in the expected areas. Even under extreme conditions, Figure 4.1.8.2 illustrates a clear formation of a stagnation point, highlighted by a red circle, as well as a slip line, underlined by a thin blue line, separating the recirculation region from the supersonic flow near the truncated base of the Aerospike. For this extreme case the pressure in the chamber was elevated to 55 atm.

        Another flow characteristic demonstrated by the benchmark flow can be seen in Figure 4.1.4.1, the formation of the envelope shock region. Between the free-stream outer jet boundary and the envelope shock, there exists a region called the envelope shock region as shown in Figure 4.1.8.3. Despite being a composition of the exhaust flow; this region appears distinguishable from the rest of the flow. This region can be seen clearly in Figure 4.1.1.2, the yellow region of flow residing immediately adjacent to the fastest moving fluid in the flow.

        Comparing results from previous studies, the benchmark Mach scene in Figure 4.1.1.2 shows the Mach number in the exhaust plume varies between Mach 1.5 and Mach 3.34. Similarly, the Mach scene from a previous Aerospike design study by Kumar [15], Figure 4.1.1.3, shows the Mach number in the exhaust plume varies between Mach 1.45 and Mach 3.54. As illustrated above, the nozzle geometry created for this study is capable of producing flow results that matches the results of a previous study and contains flow characteristics that are expected of this nozzle, with only minor differences.
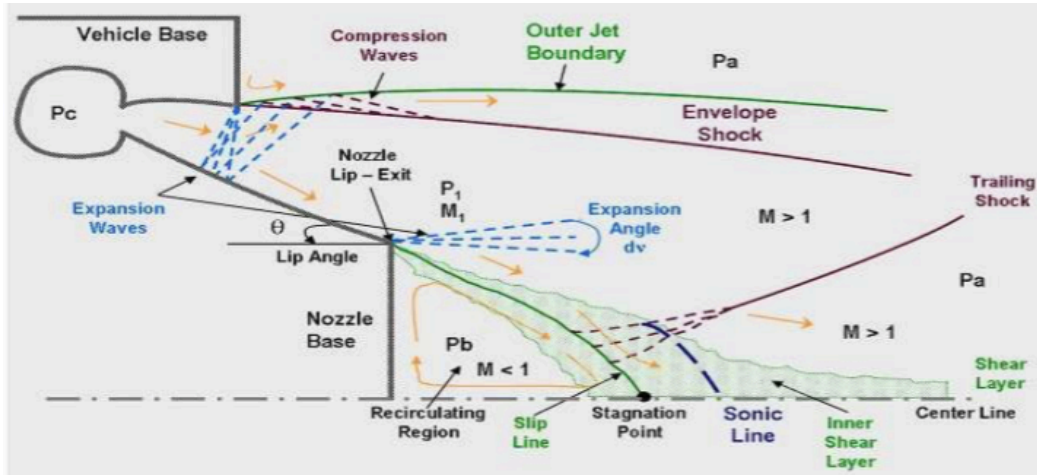
Figure 4.1.8.3 – Flow Characteristics of the Truncated Linear Aerospike [15].

4.2 Film-cooling CFD Simulation Results & Discussion

The results presented in the following section are from the simulations with added film-cooling. Evaluating the introduction of film-cooling will include plots examining Mach number, pressure, temperature, and velocity in the flow field.

4.2.1 200000 pa (3 atm) of Injection Pressure

4.2.1.1 Nozzle Performance Flow Visualization
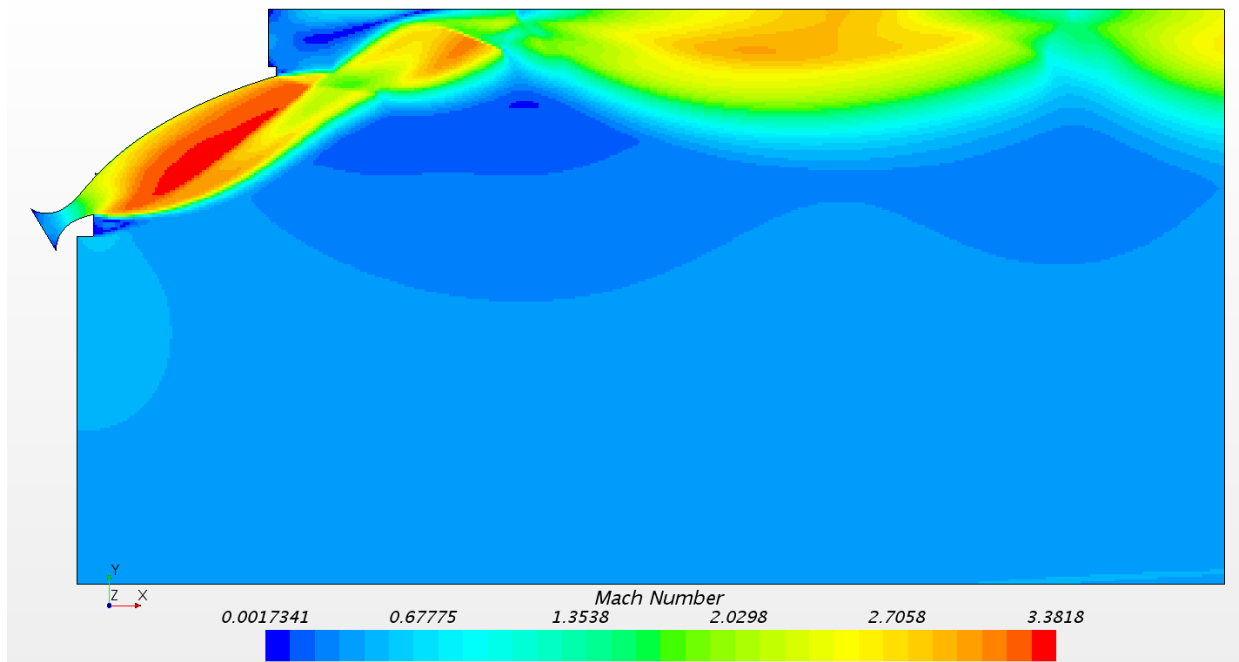
Figure 4.2.1.1.1 – Mach scene with 200,000 pa of injection pressure

4.2.1.2 Temperature
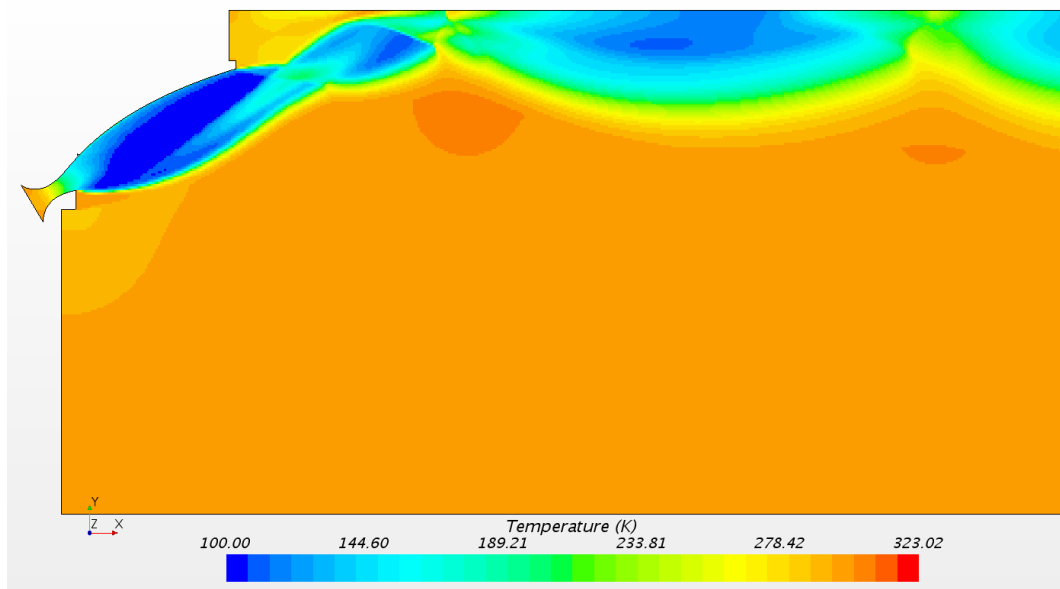
Figure 4.2.1.2.1 – Temperature scene with 200,000 pa of injection Pressure

4.2.1.3   Pressure
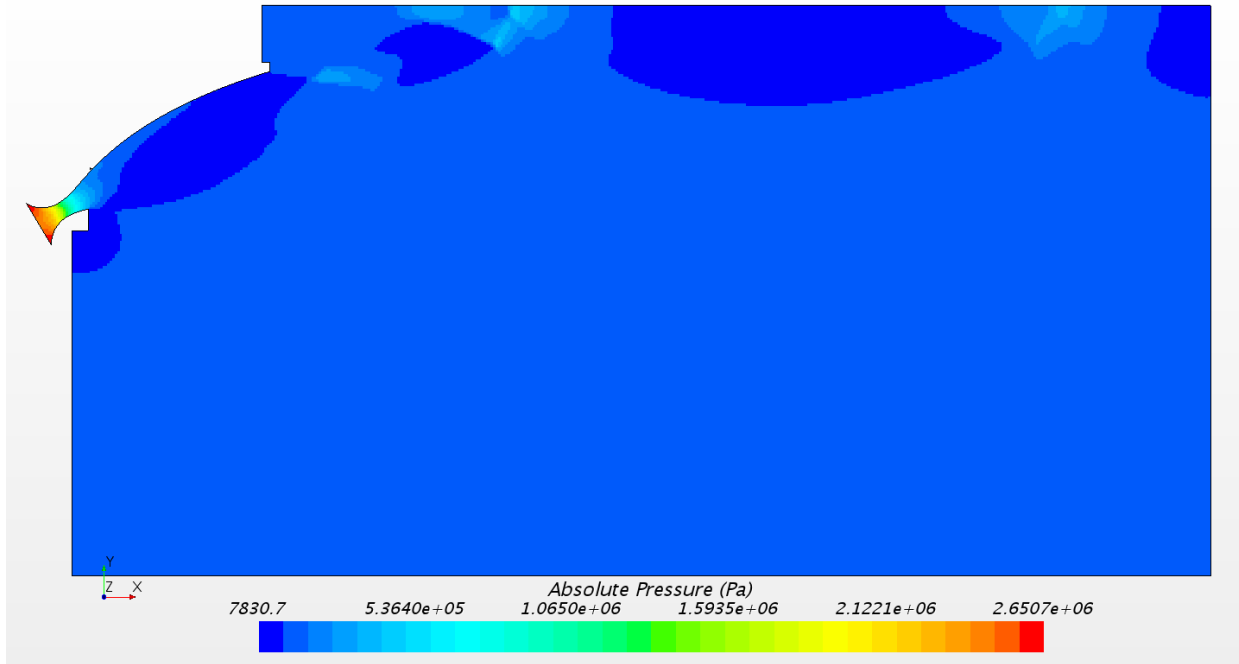
Figure 4.2.1.3.1 – Pressure scene with 200,000 pa of injection pressure

4.2.1.4   Velocity Vector
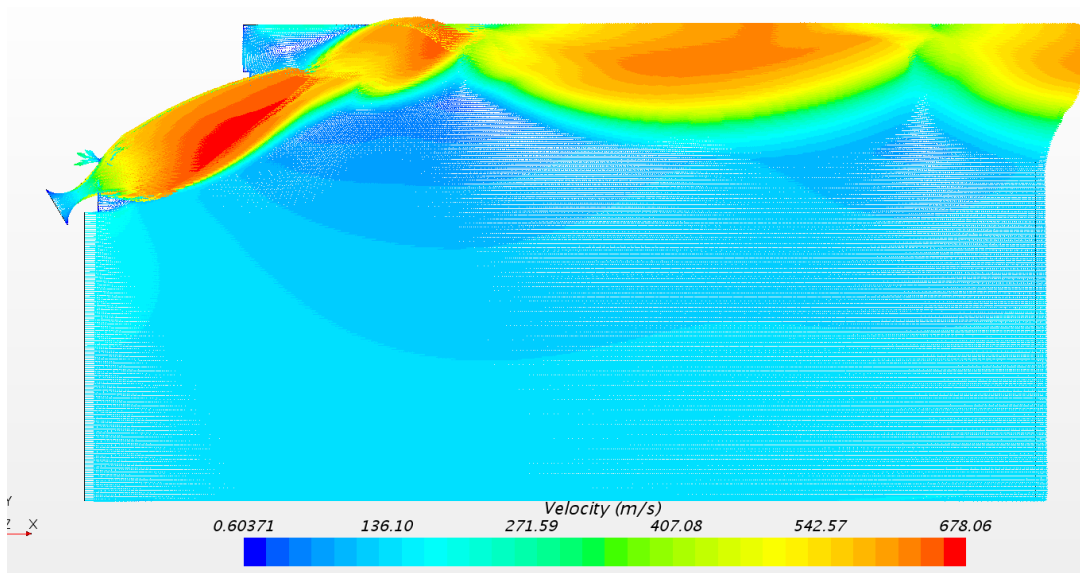
Figure 4.2.1.4.1 – Velocity vector scene with 200,000 pa of injection pressure
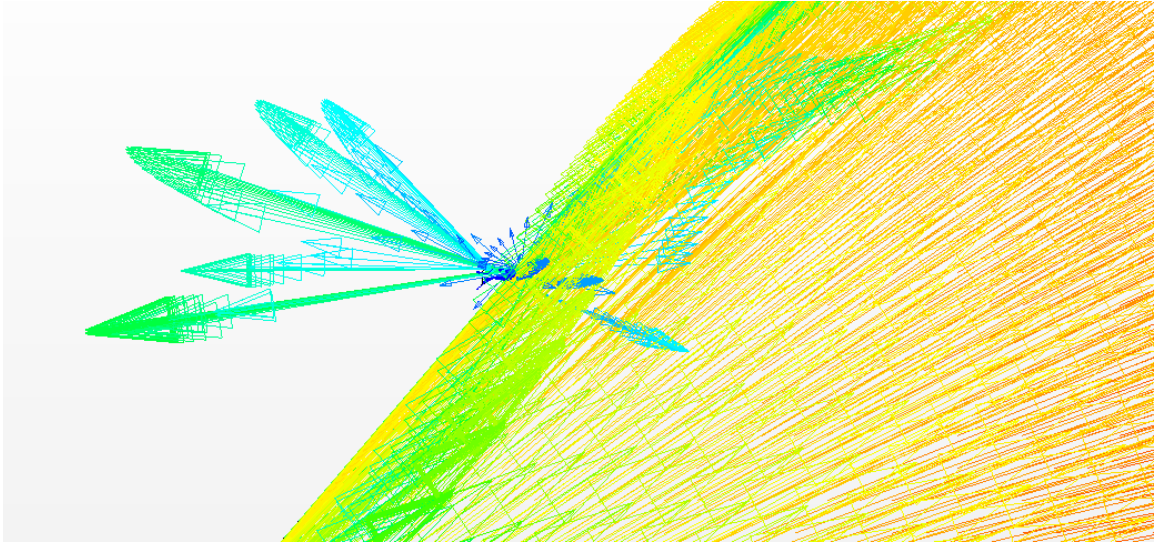
Figure 4.2.1.4.2 – Velocity vector scene with 200,000 pa of injection pressure close up of injection nozzle

4.2.2   750,000 pa (7.4 atm) of Injection Pressure

4.2.2.1   Nozzle Performance Flow Visualization
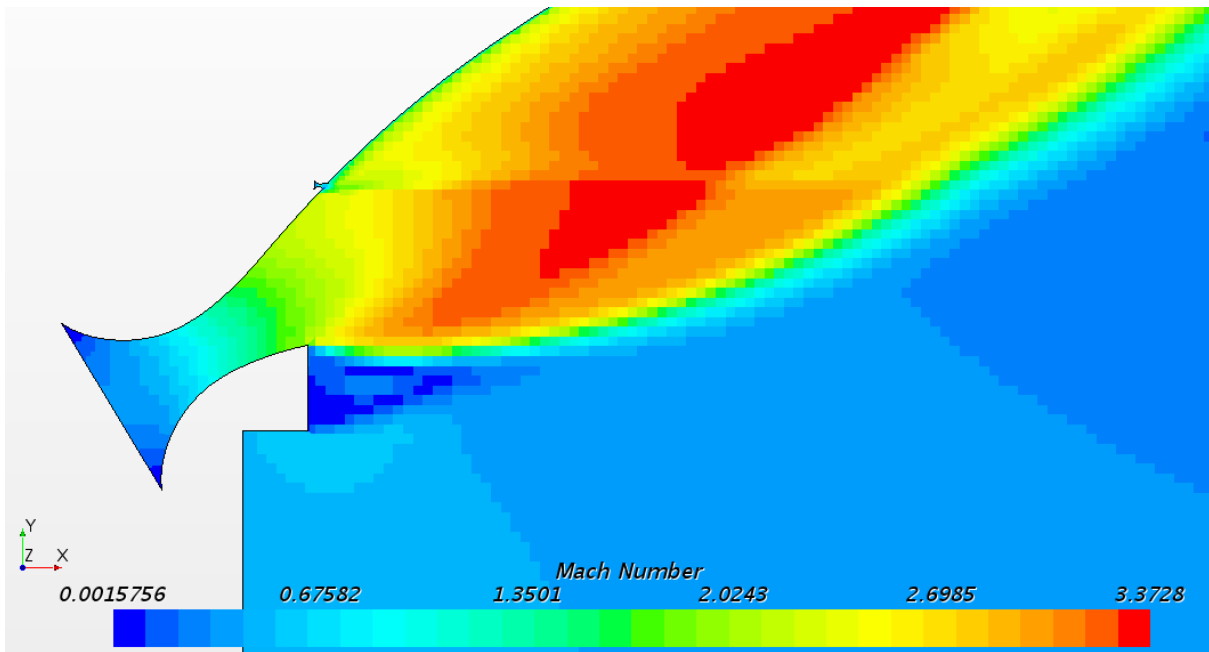
Figure 4.2.2.1.1 – Mach scene with 750,000 pa of injection pressure

4.2.2.2   Temperature
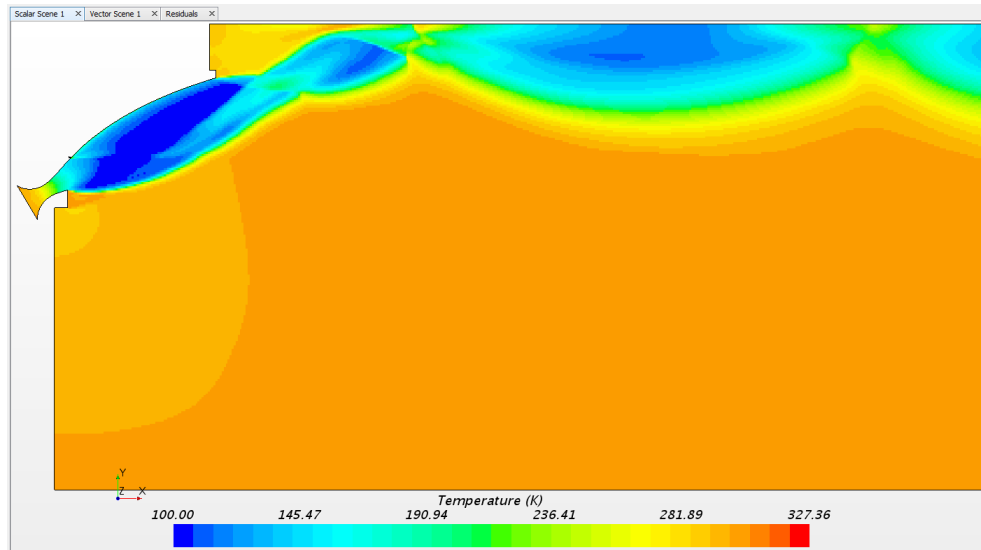
Figure 4.2.2.2.1 – Temperature scene with 750,000 pa of injection pressure

4.2.2.3   Pressure
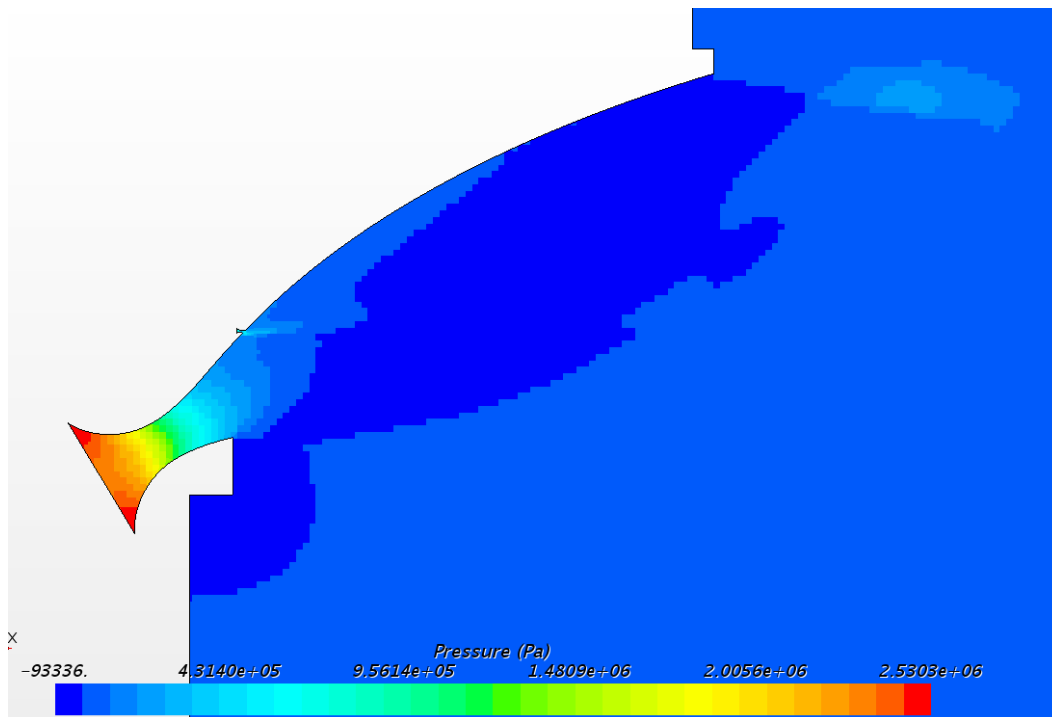
Figure 4.2.2.3.1 – Pressure scene with 750,000 pa of injection pressure

4.2.2.4   Velocity Vector
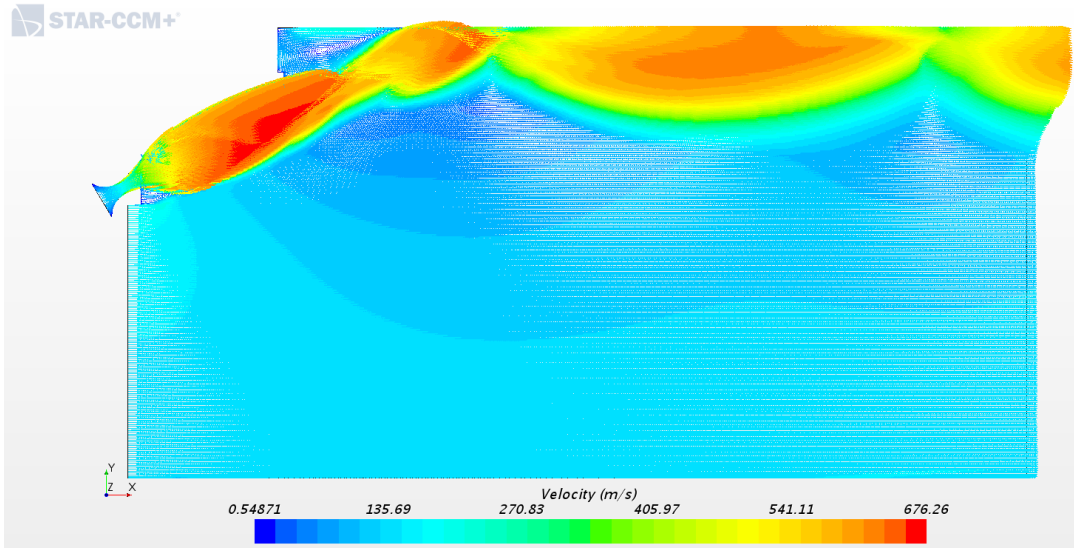
Figure 4.2.2.4.1 – Velocity vector scene with 750,000 pa of injection pressure
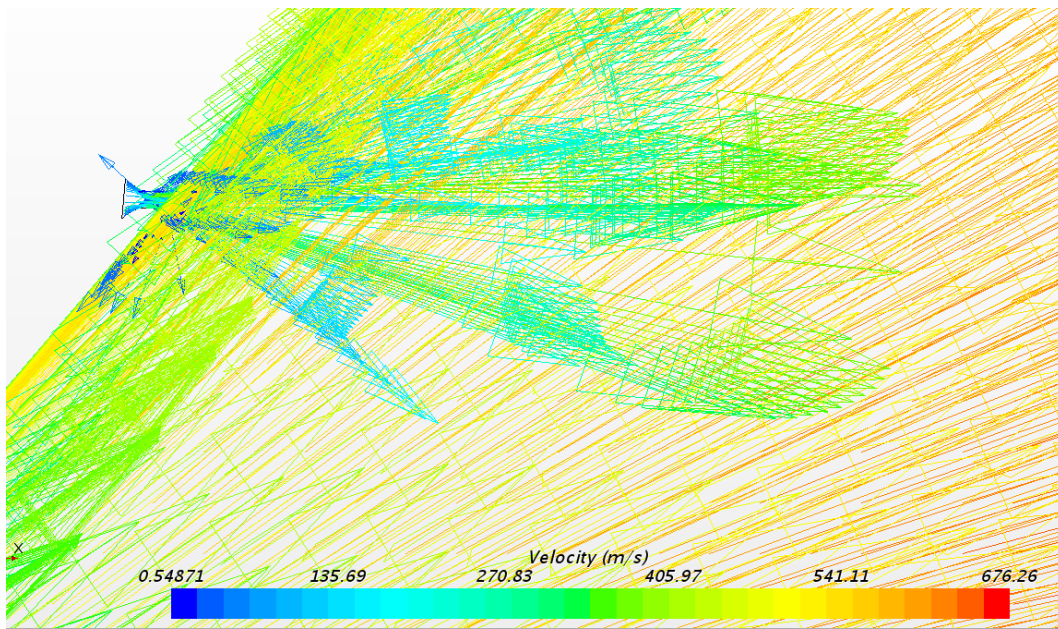
Figure 4.2.2.4.2 – Velocity vector scene with 750,000 pa of injection pressure close up of injection nozzle

4.2.3   1,000,000 pa (10 atm) of Injection Pressure

4.2.3.1   Nozzle Performance Flow Visualization
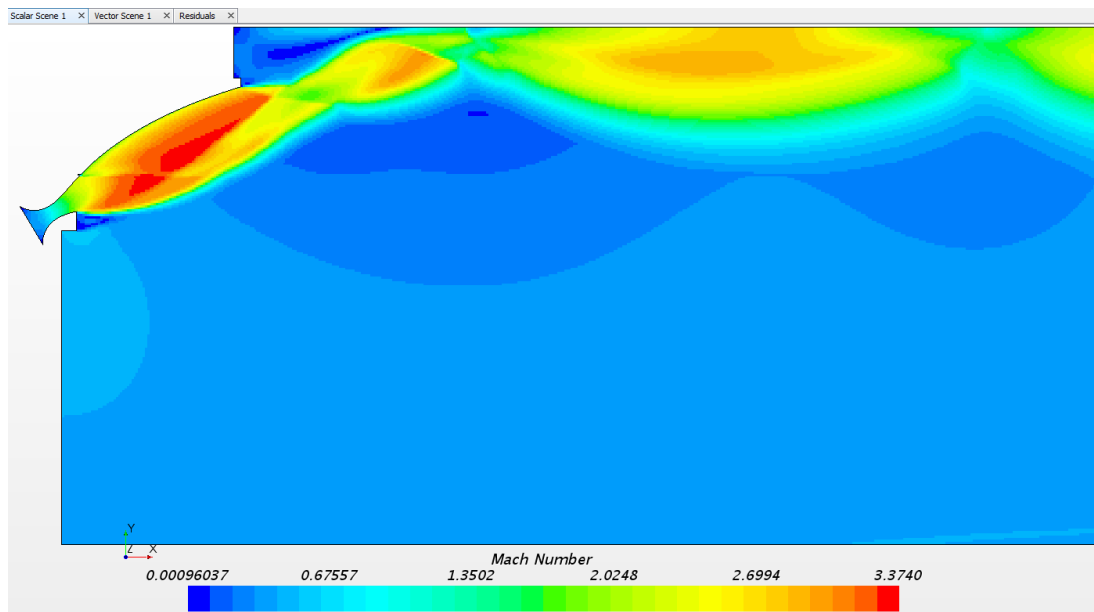
Figure 4.2.3.1.1 – Mach scene with 1,000,000 pa of injection pressure

4.2.3.2   Temperature
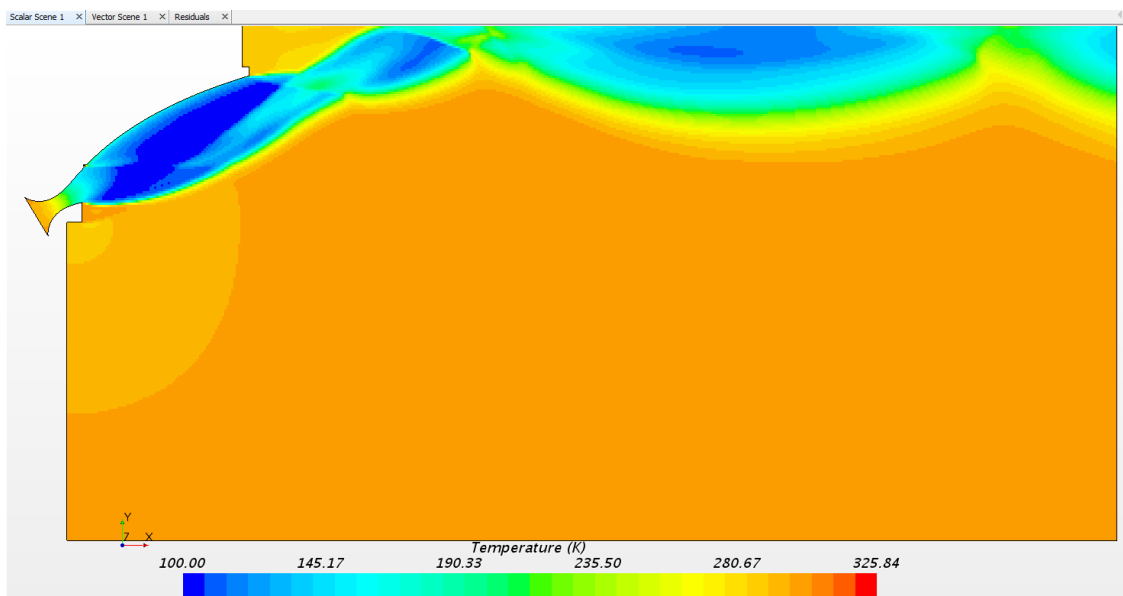
Figure 4.2.3.2.1 – Temperature scene with 1,000,000 pa of injection pressure

4.2.3.3   Pressure
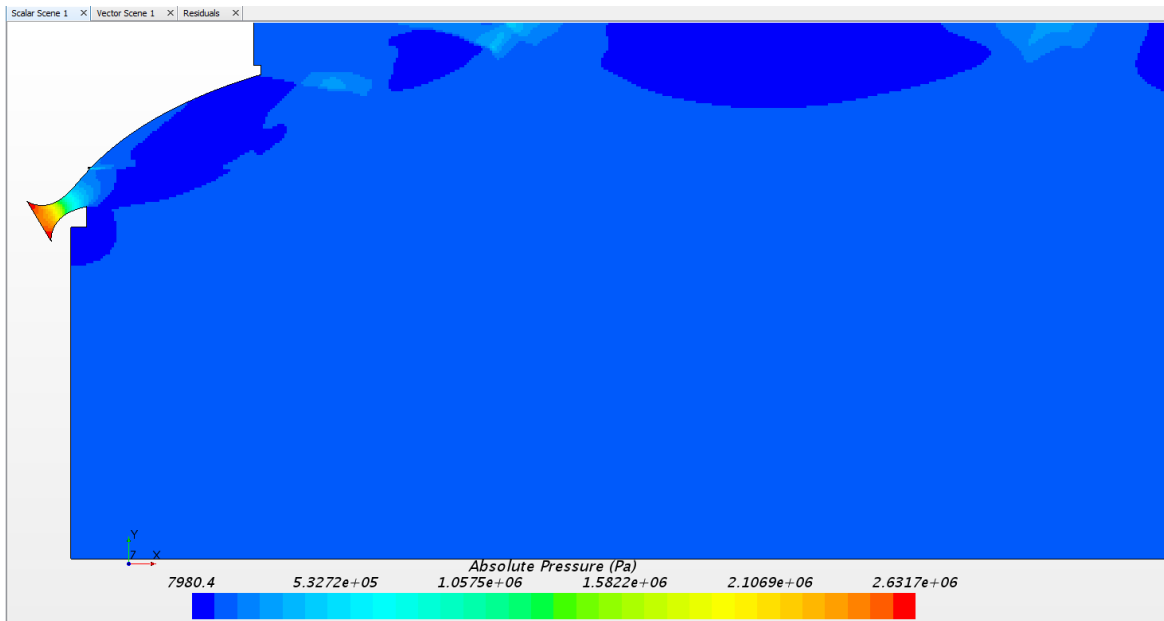
Figure 4.2.3.3.1 – Pressure scene with 1,000,000 pa of injection pressure

4.2.3.4   Velocity Vector
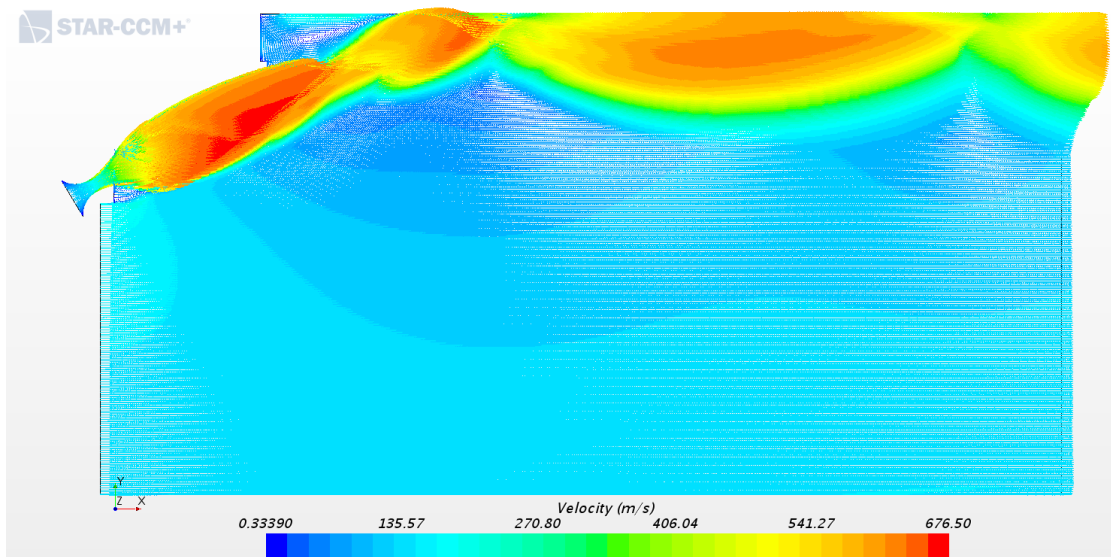
Figure 4.2.3.4.1 – Velocity vector scene with 1,000,000 pa of injection pressure
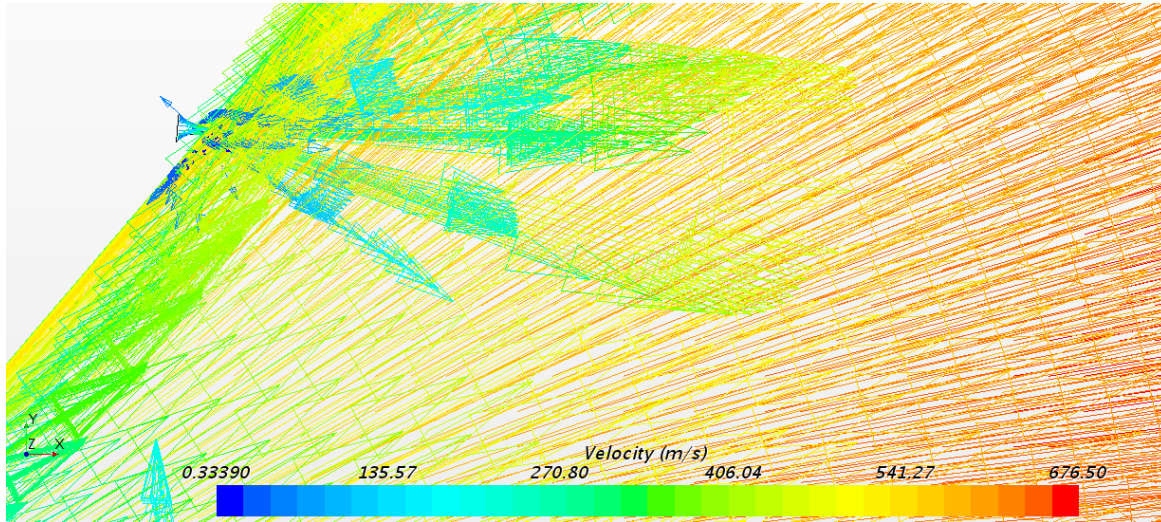
Figure 4.2.3.4.2 – Velocity vector scene with 1,000,000 pa of injection pressure close up of injection nozzle

4.3   Film-cooling Injection Discussion & Analysis

The main focus of this study was boundary formation and effect on the main exhaust flow due to the addition of a secondary flow injection. Comparing the benchmark case simulation and the Film-cooling simulations outcomes a means to evaluate the effect secondary flow injection has on the main flow. As formation of shock wave happens when slower fluid collides with the fast moving fluid emitting from the main nozzle; the pressure scenes for the medium and high injection pressure cases show a pressure increase in the flow directly downstream of the injection nozzle. Additionally, the Mach scenes for the medium and high injection pressure cases show a slowing of the flow in the same region.

With this knowledge of a pressure spike and velocity decrease, the study may sets up the potential for the formation of a shockwave. The upshot of corroborating this hypothesis shows that downstream of the pressure spike region the edge of the exhaust flow in the envelope shock region is also slowed down, altered significantly.   The Mach velocity decreases are illustrated in Figure 4.3.1a.

This information bolsters the hypothesis that a shockwave is produced as a result of introducing film-cooling. Since this shockwave is formed in the expansion section of the nozzle, the continued expansion of the exhaust flow could be potential reason for the non-traditional appearance of the shockwave. Although, this is only a hypothesis, there is no evidence in this study to support that its development in the expansion region of the nozzle being the cause of the abnormal nature of the shockwave.

Figure 4.3.1 illustrates the main exhaust flow differences between the benchmark case and the high injection pressure case. Note, the high Mach number regions differ in size. The Mach scene with high injection pressure shows a size reduction in the region of high Mach number, red and red-yellow region.   This reduction in size, though very minor, is enough to question the engines performance and the possibility the performance may be hindered. Here

lies a potential for an investigation into the thrust reduction as a piece of future work to pursue.

As mentioned above in the discussion of a potential shockwave, a byproduct of the injection cooling is a larger and minimally flared plume. This larger exhaust flow may be another source of decreased engine performance because the exhaust flow is disturbed by the flow injection. This disruption causes the plume to flare away from the rockets center line and therefore decreases efficiency.

Is there a difference between the different injection pressures/Observations of boundary layer formation?

The low injection pressure cases exhibit minimal change to the main exhaust flow, seemingly unaffected by the injection. On looking back at the benchmark Section 4.1 and low injection pressure Section 4.2.1, the Mach scene look identical in nature. The reason for the lack of a boundary layer may be evident in the figure vector scene. By looking at the direction of the flow velocity vectors it showed an inflow of fluid into the injection nozzle instead of the anticipated direction out to the exhaust plume.

Furthermore, medium and high injection pressure cases show evidence of a matured boundary layer region just aft of the injection flow nozzle. This region of slow flow near the surface remains present on the expansion ramp until roughly one-quarter and one-third of the entire length of the expansion ramp, respectively, which illustrated in Figure 46a below. After which the flow speed increases from due influence of the exhaust plume and the expansion ramp.

The injection nozzle successfully generated a boundary layer on the surface of the expansion ramp. However, this film-cooling boundary layer was insufficient in size and forms at the cost of nozzle exhaust plume performance. Noted that the thermal environment was not evaluated in this study, incorporate this element could lead to different result, perhaps!
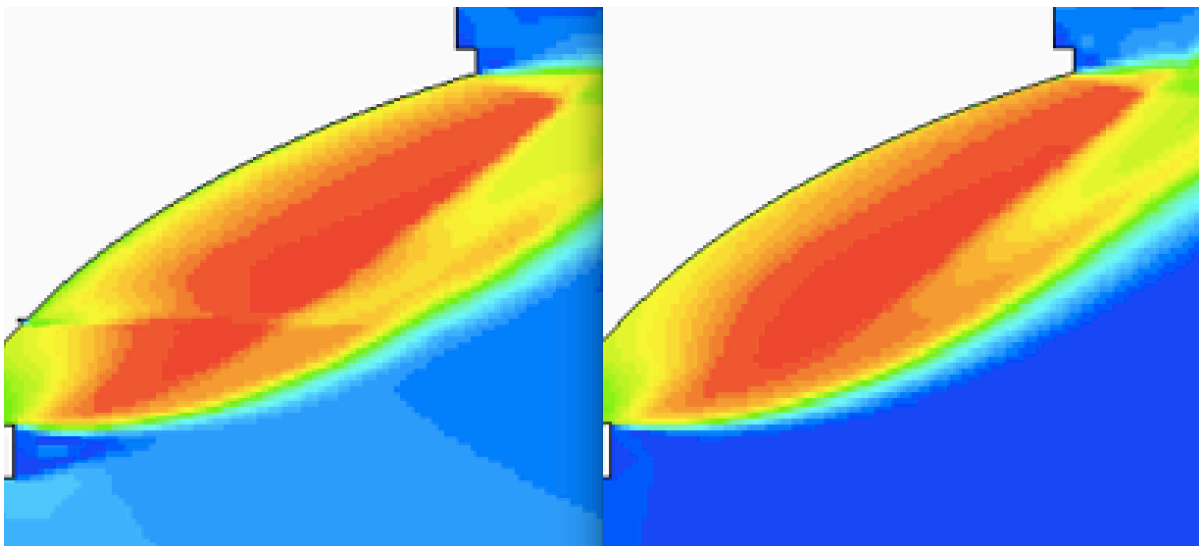
Figure 4.3.1 – Mach scene (a) High injection pressure (b) benchmark case with no injection

There is evidence that the flow is slowed down immediately aft of the injection nozzle, while the main flow maintains supersonic flow. One injection nozzle is insufficient to create

drastic change, however future work may show promise in creating a boundary layer substantial in reducing thermal flux into the expansion ramp.

5. Conclusion & Recommendation for Future Work

For this study a series of simulations of the Aerospike nozzle are performed with varied injection pressure acting on the main exhaust plume. These efforts are to explore the feasibility of using film-cooling techniques to form a boundary layer sufficient enough to provide a protective layer of fluid between the harsh thermal environments of the exhaust plume and the expansion ramp of the nozzle. The results show that equipped with singular injection nozzle, the injection of film-cooling secondary flow is insufficient to impact the boundary layer on the expansion ramp.

However, there is evidence of localized boundary layer thickening immediately aft of the flow injection location. This means future work may be warranted to improve the fidelity of the analysis. The following lists details future work:

- Thermal environments
  - o Combustion chamber environment
    - 3000k
- Injector Design of Experiment
  - o Gas composition
    - Helium, nitrogen, turbo pump exhaust composition
  - o Injection angle – with respect to the localized ramp wall.
    - $0°, 20°, 40°$
  - o Injection diameter
    - Optimize
  - o Injection quantity.
    - 3, 5, 7 along the expansion ramp surface
- Three-Dimensional CFD analysis
  - o Capture flow interactions between adjacent film-cooling injection nozzles.

Over time, evolutions in manufacturing processes and technological advances will provide solution to the issues related to the high cost to produce the Aerospike nozzle. The problems with extreme operating temperatures can be mitigated with engineering studies and solutions to remove heat from the system.

References

1. Kuyate, P., "A Review of Film-cooling; Method, Procedures, Analysis," *Sandip Institute of Technology & Research Center*, Research Gate, April, 2016.

2. Song, C., and Shen, C., "Effects of Feeding Pressures on the Flowfield Structures of Supersonic Film-cooling," *Journal of Thermophysics and Heat Transfer*, vol. 32, Dec. 2018, pp. 648–658.

3. Shewhart, A. T., Lynch, A. J., Greiner, N. J., Polanka, M. D., and Rutledge, J. L., "Mitigation of Heat Release from Film-cooling in Fuel-Rich Environments," *Journal of Propulsion and Power*, vol. 32, Jun. 2016, pp. 1454–1461.

4. Hombsch, M., and Olivier, H., "Film-cooling in Laminar and Turbulent Supersonic Flows," *Journal of Spacecraft and Rockets*, vol. 50, Jul. 2013, pp. 742–753.

5. Bills, J. D., Crowe, D. S., Rutledge, J. L., and Coy, E. B., "Modeling Fuel Film-cooling on a Flat Plate," *Journal of Thermophysics and Heat Transfer*, vol. 32, Jul. 2018, pp. 736–746.

6. Schneider, D., Stark, R. H., Genin, C., Oschwald, M., and Kostyrkin, K., "Operation Mode Transition of Film-Cooled Dual-Bell Nozzles," *2018 Joint Propulsion Conference*, vol. 28, Aug. 2018, pp. 517–529.

7. Street, R. D., "Effects of Injection Nozzle Configuration on Secondary Injection Into Supersonic Flow," *In Partial Fulfillment of the Requirements For the Degree of Mechanical Engineer California Institute of Technology Pasadena*, California, 1966.

8. Spaid, F., "Secondary Injection of Gases Into a Supersonic Flow," *Solid Propellant Rocket Conference*, vol. 2, Oct. 1964, pp. 1689–1696.

9. Wang, T.-S., "Analysis of Linear Aerospike Plume Induced Base-Heating Physics and Fence Effect," *33rd Thermophysics Conference*, vol. 14, 1999, pp. 457–463.

10. Takahashi, H., "Performance Evaluation of Airframe-Integrated Aerospike Propulsion Systems in Off-Design Flight Conditions," *Journal of Propulsion and Power*, vol. 32, Mar. 2016, pp. 408–419.

11. Sutton, G. P., and Biblarz, O., *Rocket propulsion elements*, Hoboken: John Wiley & Sons, 2017.

12. Pasha, A. A., and Sinha, K., "Shock-Unsteadiness Model Applied to Oblique Shock Wave/Turbulent Boundary-Layer Interaction," *International Journal of Computational Fluid Dynamics*, vol. 22, Sep. 2008, pp. 569–582.

13. Sandham, D. N., "Shock-Wave/Boundary-Layer Interactions," Aerodynamics and Flight Mechanics Research Group, Southampton, UK.

14. Borovoy, V. Y., Egorov, I. V., Skuratov, A. S., and Struminskaya, I. V., "Two-Dimensional Shock-Wave/Boundary-Layer Interaction in the Presence of Entropy Layer," *AIAA Journal*, vol. 51, Jan. 2013, pp. 80–93.

15. Kumar, K. N., Gopalsamy, M., Antony, D., Krishnaraj, R., and Viswanadh, C. B. V., "Design and Optimization of Aerospike nozzle using CFD," *IOP Conference Series: Materials Science and Engineering*, vol. 247, 2017, p. 012008.

16. Corda, S., Neal, B., Moes, T., Cox, T., Monaghan, R., Voelker, L., Corpening, G., Larson, R., Powers, B., Flight testing the Linear Aerospike SR-71 Experiment (LASRE), *NASA/TM-1998-206567*, 1998.

17. Lash, E., "Trajectory Analysis and Comparison of a Linear Aerospike Nozzle to a Convensional Bell Nozzle for SSTO Flight", *Masters Theses*, University of Tennessee, 2015

18. Wang, T.-S., "Analysis of Linear Aerospike Plume-Induced X-33 Base-Heating Environment," *Journal of Spacecraft and Rockets*, vol. 36, 1999, pp. 777–783.

19. Wendt, J. F., and Anderson, J. D., *Computational fluid dynamics: an introduction ;*Berlin: Springer, 2009.

20. Bani, Abdalla Ali, "Design and Analysis of an Axisymmetric Aerospike Supersonic Micro-Nozzle for a Refrigerant-Based Cold-Gas Propulsion System for Small Satellites" (2016). *Masters Theses*. 7591.

Appendix A – Expansion Ramp Contour MATLAB Script

```
% Functions used: - Mach2AR, AR2Mach (convert between Area ratio and Mach)
% - Mach2Prandtl (convert from Mach to Prandtl-Meyer angle)
% - Mach2Mangle (convert Mach to Mach angle)
%_____ % note:
these coordinates are revolved around the central axis to obtain
% the 3-D spike
%_____ % all
non-dimensional values are non-dimensionalized by [r_e] the exit
% radius of the spike (see Figure 1b. in the Reference)
% - ratio of specific heats [gamma]
% - non-dimensional radius at end of spike [eta_b] (zero for a non-truncated spike)

AR = 3.5;
%AR = 40
gamma = 1.1251;
eta_b = 0.5;

% input tube inner diameter (the units of this parameter determine the units of the
dimensional results)
t_diam = input('input value of tube diameter: \n');
A_t = pi*((t_diam/2)^2); % throat area
A_e = AR*A_t;
r_e = sqrt(A_e/pi);
```

```matlab
M_e = AR2Mach(AR,gamma);
nu_e = Mach2Prandtl(M_e,gamma);
N = 10000000;
M_vals = linspace(1,M_e,N);
AR_vals = Mach2AR(M_vals,gamma); %Area Ratio
nu_vals = Mach2Prandtl(M_vals,gamma);
mu_vals = Mach2Mangle(M_vals);
alpha_vals = nu_e-nu_vals+mu_vals;
% non-dimensional values
l_nondim_vals = (1-sqrt(1-(AR_vals.*(1-
(eta_b.^2)).*M_vals.*(sin(alpha_vals)./AR))))./sin(alpha_vals);
r_nondim_vals = 1-(l_nondim_vals.*sin(alpha_vals));
x_nondim_vals = l_nondim_vals.*cos(alpha_vals);
y_nondim_vals = l_nondim_vals.*sin(alpha_vals);
Length_nondim = max(x_nondim_vals)-min(x_nondim_vals);
% dimensional values
l_vals = l_nondim_vals.*r_e;

r_vals = r_nondim_vals.*r_e;
x_vals = x_nondim_vals.*r_e;
y_vals = y_nondim_vals.*r_e;
Length = Length_nondim.*r_e;
%Plotting
figure
plot(r_nondim_vals,x_nondim_vals);
xlabel('r/r_e')
ylabel('x/r_e')
figure
plot(x_nondim_vals,y_nondim_vals,0,0,'o');
xlabel('x/r_e')
ylabel('y/r_e')
fprintf('Exit Mach number = %g \n',M_e)
fprintf('Length = %g [in] \n',Length)
fprintf('Cowl Seperation = %g [in] \n \n',min(l_vals))
fprintf('Flow Turn Angle = %g [deg] \n',nu_e*180/pi)

% Create a text file containing coordinates for input in CAD
n = 500;
m = N/n;
p = length(x_vals);
x = x_vals(1:m:p);
y = y_vals(1:m:p);
z = zeros(1,n);
A = [x;y;z];
fileID = fopen('Aerospike_contour_2.txt','w');
fprintf(fileID,'%6.10f %12.10f %12.10f\n',A);
fclose(fileID);

% Mach number to area ratio (AR)
function [AR] = Mach2AR(M,gamma)
f1 = 2/(gamma+1);
f2 = (gamma-1)/2;
f3 = (gamma+1)/(gamma-1);
AR = sqrt((1./(M.^2)).*((f1.*(1+(f2.*(M.^2)))).^f3));
end

function [nu] = Mach2Prandtl(M,gamma)
```

```
f1 = (gamma+1)/(gamma-1);
f2 = 1/f1;
nu = sqrt(f1).*atan(sqrt((f2.*((M.^2)-1))))-atan(sqrt((M.^2)-1));
end
```

Appendix B – Gas Sonic Velocity Calculator MATLAB Script

```
% Velocity calculator
%MW=(2.015+5.5*(2*15.999)) % amu
MW=12.80 %  from CEA
% or
% MW=12.65
R=(8314.45)/MW % j/kg-k
R_=R*5.97994 % ft lbf/slug °R
T=1597.422222 % k
%T=3255.37 % k
T_=2875.3599996 % °R
gamma=1.15 %  from CEA
sonvelocity=1561.7 %  from CEA m/s
Speedofsound=sqrt(gamma*R*T) % m/s
exitvelocity=2.5*Speedofsound % m/s
exitvelocity_=3.281*exitvelocity % ft/s
MW = 12.8000
R= 649.5664
R_ =
   3.8844e+03
T= 1.5974e+03
T_ =
   2.8754e+03
gamma =
    1.1500
sonvelocity = 1.5617e+03
        Speedofsound =
          1.0924e+03
        exitvelocity =
          2.7309e+03
        exitvelocity_ =
          8.9602e+03
```

```
1 Helium 2 Nitrogen 3 Combuster gases:
inject1MW=4.003;
inject2MW=28.013;
inject3MW=MW;
inject1R=(8314.45)/inject1MW
inject2R=(8314.45)/inject2MW
inject3R=(8314.45)/inject3MW
injectT1=200;
injectT2=200;
injectT3=1597.42;
injectorgamma1=1.66;
injectorgamma2=1.40;
injectorgamma3=1.150;
injectionnozvel1=1/4*exitvelocity_ % ft/s
injectionnozvel2=2/4*exitvelocity_ % ft/s
injectionnozvel3=3/4*exitvelocity_ % ft/s
sonicvel1_1=sqrt(injectorgamma1*(inject1R)*(injectT1))  % ft/s
sonicvel1_2=sqrt(injectorgamma2*(inject2R)*(injectT2))  % ft/s
sonicvel1_3=sqrt(injectorgamma3*(inject3R)*(injectT3))  % ft/s
injnozexitvelocity1_1=(1/4)*sonicvel1_1
injnozexitvelocity2_1=(2/4)*sonicvel1_1
injnozexitvelocity3_1=(3/4)*sonicvel1_1
injnozexitvelocity1_2=(1/4)*sonicvel1_2
injnozexitvelocity2_2=(2/4)*sonicvel1_2
injnozexitvelocity3_2=(3/4)*sonicvel1_2
injnozexitvelocity1_3=(1/4)*sonicvel1_3
injnozexitvelocity2_3=(2/4)*sonicvel1_3
injnozexitvelocity3_3=(3/4)*sonicvel1_3
```